

ACTA MATERIALIA TRANSYLVANICA

Material Sciences Publications

Volume 7, Issue 1



ERDÉLYI MÚZEUM-EGYESÜLET
Kolozsvár
2024

A folyóirat megjelenését támogatta a Communitas Alapítvány, a Magyar Tudományos Akadémia, a Bethlen Gábor Alapkezelő Zrt. és az EME Műszaki Tudományok Szakosztálya / The publication of this magazine was supported by the Communitas Foundation, by the Hungarian Academy of Sciences, by the Bethlen Gábor Fund and by the TMS – Department of Engineering Sciences.



Főszerkesztő / Editor-in-Chief: Bitay Enikő

Nemzetközi Tanácsadó testület / International Editorial Advisory Board:

Prof. Biró László Péter, MTA Energiatudományi Kutatóközpont, Budapest, Magyarország
 Prof. emer. B. Nagy János, University of Namur, Namur, Belgium
 Prof. Czigány Tibor, Budapesti Műszaki és Gazdaságtudományi Egyetem, Budapest, Magyarország
 Prof. Diószegi Attila, Jönköping University, Jönköping, Svédország
 Dobránszky János, HUN-REN Kompozittechnológiai Kutatócsoport, Budapest, Magyarország
 Prof. Dusza János, Institute of Materials Research of Slovak Academy of Sciences, Kassa, Szlovákia
 Prof. Kaptay György, Miskolci Egyetem, Miskolc, Magyarország
 Dr. Kolozsváry Zoltán, Plasmaterm Rt., Marosvásárhely, Románia
 Prof. Mertinger Valéria, Miskolci Egyetem, Miskolc, Magyarország
 Prof. Porkoláb Miklós, Massachusetts Institute of Technology, Cambridge, MA, USA
 Prof. Réger Mihály, Óbudai Egyetem, Budapest, Magyarország
 Prof. emer. Réti Tamás, Óbudai Egyetem, Budapest, Magyarország
 Prof. emer. Roósz András, Miskolci Egyetem, Miskolc, Magyarország
 Dr. Spenik Sándor, Ungvári Nemzeti Egyetem, Ungvár, Ukrajna
 Prof. Zsoldos Ibolya, Széchenyi István Egyetem, Győr, Magyarország

Lapszámszerkesztők / Editorial Board:

Dobránszky János, HUN-REN Kompozittechnológiai Kutatócsoport, Budapest, Magyarország
 Csavdári Alexandra, Babeş-Bolyai Tudományegyetem, Kolozsvár, Románia
 Gergely Attila, Sapientia Erdélyi Magyar Tudományegyetem, Marosvásárhely, Románia
 Kovács Tünde, Óbudai Egyetem, Budapest, Magyarország

Kiadó / Publisher: Erdélyi Múzeum-Egyesület

Felelős kiadó / Responsible publisher: Biró Annamária

Olvasószerkesztő / Proofreader: Szenkovics Enikő (magyar), David Speight (English)

Szerkesztőségi titkár / Editorial secretary: Kisfaludi-Bak Zsombor

Borítóterv / Cover: Kőnczey Elemér

Nyomdai munkálatok / Printed at: F&F International Kft., Gyergyószentmiklós

Copyright © a szerzők / the authors, EME/ TMS 2024

ISSN 2601-1883, ISSN-L 2601-1883

DOI: 10.33923/amt-2024-01

A folyóirat honlapja: <https://www.eme.ro/publication-hu/acta-mat/mat-main.htm>

The journal website: <https://www.eme.ro/publication/acta-mat/mat-main.htm>

Az *Acta Materialia Transylvanica. Anyagtudományi Közlemények* az Erdélyi Múzeum-Egyesület (EME) Műszaki Tudományok Szakosztályának folyóirata, amely az anyagtudományok területéről közlő tudományos közleményeket: szakcikkeket, összefoglalókat (szemléket), tanulmányokat. A folyóirat célja összképet adni kiemelten a Kárpát-medencei kutatási irányokról, tudományos eredményeiről, s ezt széles körben terjeszteni is. A folyóirat az EME felvállalt céljaihoz híven a magyar szaknyelv ápolását is támogatja, így a nyomtatott folyóirat magyar nyelven jelenik meg, mely az Erdélyi digitális adattárban elérhető (<https://eda.eme.ro/handle/10598/30356>). A széles körű nemzetközi terjesztés érdekében a folyóirat teljes angol nyelvű változatát is közzétesszük.

Acta Materialia Transylvanica – Material Sciences Publications – is a journal of the Technical Sciences Department of the Transylvanian Museum Society, publishing scientific papers, issues, reviews and studies in the field of material sciences. Its mission is to provide and disseminate a comprehensive picture focusing on research trends and scientific results in the Carpathian basin. In accordance with the general mission of the Transylvanian Museum Society it aims to support specialized literature in Hungarian. The printed version of the journal is published in Hungarian and is available in the Transylvanian Digital Database (<https://eda.eme.ro/handle/10598/30356>). However, we would like to spread it internationally, therefore the full content of the journal will also be available in English.

Tartalom / Content

BOGNÁR ADRIÁN, LEDNICZKY GYÖRGY, KUN KRISZTIÁN, ZSIDAI LÁSZLÓ	1
<i>Szálkisajtolással előállított, 1.4542 típusú korrózióálló acél próbatetek mikroszerkezeti vizsgálata</i>	
<i>Microstructural Characterization of 1.4542 Type Stainless Steel Specimens Manufactured by Fused Filament Fabrication</i>	
BORBÉLY RICHÁRD, KÖLÜS MARTIN LÁSZLÓ, BÉRES GÁBOR JÓZSEF	8
<i>Járműkarosszéria-lemezek alakítási tulajdonságainak vizsgálata</i>	
<i>Examination of the Forming Properties of Vehicle Body Panels</i>	
BREZNAY CSABA, VARBAI BALÁZS	14
<i>Auszténites korrózióálló acélok lézeres hegesztési varratainak korróziós vizsgálata</i>	
<i>Corrosion Testing of Laser Welded Austenitic Stainless Steel Welds</i>	
JUHÁSZ ZSOMBOR, RENKÓ JÓZSEF BÁLINT	18
<i>Többtengelyű kovácsolással alakított rézminták mikrokeménységének vizsgálata</i>	
<i>Investigation of Microhardness of Multiaxially Forged Copper Samples</i>	
KÖLÜS MARTIN LÁSZLÓ, BORBÉLY RICHÁRD, BÉRES GÁBOR JÓZSEF	24
<i>A karcsúsági viszony hatása a síkbeli alakváltozásra halmaznyomó vizsgálatok során</i>	
<i>Effect of the Slenderness Relation on in-plane Deformation in Stack Compression Tests</i>	
MÁRTON PÉTER	29
<i>A 3PHV60 típusú műgyanta alkalmazása a faszervezetek javítására</i>	
<i>Application of 3PHV60 Type Epoxy Resin for the Repair of Timber Structures</i>	
OLÁH KLAUDIA, KORSÓS KRISZTIÁN, KOVÁCS DORINA	39
<i>Eltérő nitridálási eljárásokkal kezelt melegalakító szerszámacél vizsgálata ciklikus hőterhelést követően</i>	
<i>Examination of a Hot-Work Tool Steel Treated with Different Nitriding Processes after Cyclic Heating</i>	

SIMON VIRÁG, VARBAI BALÁZS, ABAFFY KÁROLY, GYURA LÁSZLÓ	44
<i>A teljesítmény és a haladási sebesség hatása a varratgeometriára kézi lézeres hegesztés esetén</i>	
<i>The Effects of Laser Power and Travel Speed on Weld Geometry in the case of Manual Laser Welding</i>	
STADLER RÓBERT GÁBOR, HORVÁTH RICHÁRD	48
<i>Polikarbonátlemezek kavardörzs-hegesztett kötésének vizsgálata</i>	
<i>Investigation of Friction Stir Welded Polycarbonate Plates</i>	
SZABÓ VALENTIN ENDRE, KUN KRISZTIÁN	54
<i>Üvegszál-erősítésű, pultrudált műanyag profilk csavarkötésének roncsolásos vizsgálata</i>	
<i>Tensile Testing of Bolted Joints in Pultruded Glass Fibre Reinforced Plastic Profiles</i>	



Microstructural Characterization of 1.4542 Type Stainless Steel Specimens Manufactured by Fused Filament Fabrication

Adrián BOGNÁR,^{1*} György LEDNICZKY,¹ Krisztián KUN,¹ László ZSIDAI²

^{1*} John von Neumann University, GAMF Faculty of Engineering and Computer Science, Department of Innovative Vehicles and Materials, Kecskemét, Hungary, bognar.adrian@nje.hu

² Hungarian University of Agriculture and Life Sciences, Szent István Campus, Institute of Technology, Department of Materials Science and Engineering Processes, Gödöllő, Hungary

Abstract

The processes of design and manufacturing continue to expand with extraordinary opportunities due to the emergence and development of additive manufacturing technologies. Additive manufacturing processes radically differ from traditional manufacturing methods and require a completely new engineering approach. As a result, new possibilities emerge, allowing the creation of geometries that were previously difficult or impossible to produce using other technologies. Significant application opportunities exist in fields such as medicine and many sectors of industry due to this advancement. The range of materials used in additive manufacturing is constantly improving and expanding, although the most significant results are in the area of industrial applicability, which is the focus of this research. It is important to mention that besides Selective Laser Sintering / Selective Laser Melting (SLS / SLM), Fused Filament Fabrication (FFF) is worth considering for producing metal parts, due to lower costs and the possibility of manufacturing larger parts. The aim of the research is to examine the microstructural and macrostructural characteristics of finished components produced by FFF.

Keywords: *additive manufacturing, material extrusion, stainless steel, microstructural characterization.*

1. Introduction

Additive manufacturing of metal products is increasingly common in the production of automotive parts and medical prosthetics, thanks to a wide range of processes and materials. These processes require significant investment and complex equipment to ensure the safe handling of metal powder with minimal health risks. The metal powders used in processes branded as SLS® (Selective Laser Sintering) or DMLS (Direct Metal Laser Sintering) have particle sizes ranging from 15 to 50 μm , posing similar health risks to operators as welding [1, 2]. Among other reasons, these health risks, along with the substantial investment costs and laser-related safety concerns, have spurred multiple research directions that employ new methods for the additive manufacturing of metal parts [3].

1.1. Additive Manufacturing of metal materials

Among the seven types of additive manufacturing processes defined by the ISO 52900-1 terminology standard, one variant of material extrusion is fused filament fabrication (FFF). The first step in filament-based metal printing involves producing green parts. These components have not yet undergone the debinding and sintering processes. While they are accurate in shape and size, their surface roughness and density are not as well regulated as in laser processes. After the debinding process, the green parts require the most attention and are referred to as brown parts due to their characteristic color at this stage. These parts are porous, brittle, and lack the binder that helps hold them together. According to previous literature reviews, this process has limitations due to

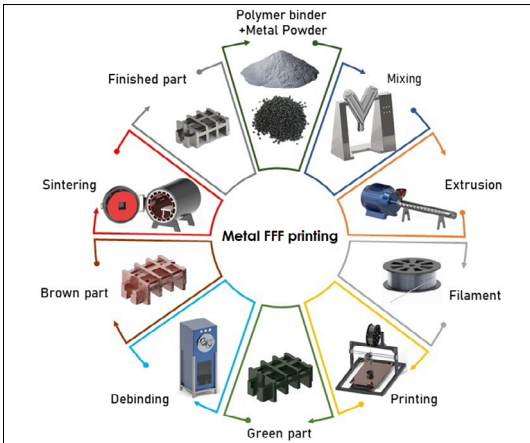


Fig. 1. The process of metal FFF printing.

the strength of the test specimens, as the internal parts require a minimum level of infill [1, 3].

The FFF process is simple to perform and requires minimal investment compared to other additive manufacturing processes. Another advantage is that when producing complex parts, there is no need to create channels to remove unused powder from the work area [4, 5, 6].

Figure 1. illustrates the process of producing metal parts based on filament-based technology.

1.2. Post-processing techniques

As mentioned in the previous paragraph, the green parts produced in this way require further treatments to obtain test specimens with properties nearly identical to those made from solid materials [1, 3].

During these treatments, the first step is to remove the binder. The resulting brown parts must then be sintered at high temperatures. If necessary, additional processes, such as heat treatment or hot isostatic pressing, can be performed to enhance mechanical properties [4, 5].

There are three main methods for binder removal:

- solvent-based: using trichloroethane or heptane;
- thermal: applying a temperature range of 60–600°C;
- catalytic: using nitric acid or oxalic acid at temperatures between 110–150°C [7].

After binder removal, the brown parts reach their final state through high-temperature sintering, undergoing a shrinkage of 10–20% compared to the green part. To compensate for this, it is crucial to focus on appropriate scaling settings

during the design phase. The dimensions of the test specimens need to be increased to varying extents in the X, Y, and Z directions. The necessary values are provided by the manufacturer of the filler material [8].

During sintering, six mechanisms of material transport are distinguished:

- surface diffusion;
- lattice diffusion;
- grain boundary diffusion;
- evaporation and condensation;
- viscous flow;
- plastic flow [9].

After the sintering process, the porosity of the workpieces is expected to be between 10–20%, depending on the temperature applied. Nitrogen, argon, and hydrogen can be used as protective gases during sintering. Several factors influence the sintering process:

- heating rate;
- sintering temperature;
- sintering process duration;
- furnace atmosphere [10].

2. The methodology of the experiment

The printing was done using BASF Ultrafuse 17-4PH filament. This type of filler material is one of the most common in metal printing literature. Essentially, it is a composite filament produced by extruding a blend of 1.4542 grade stainless steel powder and a binder. The key characteristics related to the processing conditions of this printing filler material are shown in Table 1.

Table 1. Recommended processing parameters for BASF Ultrafuse 17-4PH filament [8]

Recommended processing parameters	
Nozzle temperature	230–250 °C
Bed temperature	90–100 °C
Nozzle diameter	≥0,4 mm
Printing speed	15–50 m/s
Cooling	nem
Scaling of specimens	X and Y direction: 119% Z direction: 122%

To produce the green parts, we used a Craft-Bot Flow Idex XL 3D printer operating on filament-based technology.

2.1. The modified manufacturing parameters

During the experiment, test specimens commonly used in Metal Injection Molding (MIM) were printed with modified settings [11].

Each piece was printed with 100% infill and oriented in the X-Y plane. Three parameters were selected as variables in the CraftWare slicing software, based on previous literature findings, which could impact mechanical properties and printing time:

- layer thickness (mm);
- printing speed (mm/s);
- infill orientation (°) [12, 13, 14].

Printing speed fundamentally affects the movement speed of the printer head, thus influencing printing time. However, it may also influence the degree of adhesion between layers, potentially affecting tensile strength [15, 16, 17].

Preliminary experiments indicated that printing speed needed to be reduced, so its values had to be chosen from a lower range.

Table 2. The various printing parameters used for manufacturing the test specimens

Experiment	Layer height (mm)	Printing speed (mm/s)	Infill orientation (°)
#1	0,2	25	45
#2	0,3	15	45
#3	0,4	35	45

The green part is shown in the Figure 2.

2.2. Binder removal and sintering

Materials composed of different metal powders and binder systems require varied binder removal and sintering technologies and atmospheres, so in this experiment we enlisted the services of Elnik System GmbH [18].

In the binder removal cycle, the specimens are initially preheated to 120 °C at a low heating rate. Initially, the rate is set to 5 °C, then reduced to 1 °C, and finally to 0.5 °C per minute. Once 120°C is reached, they are held at this temperature for 45 minutes. Subsequently, the acid flow begins, lasting for one hour per 1 mm of wall thickness. The flow rate of the acid is 3.4 ml per minute. After the acid flow is complete, the specimens are held at 120 °C for 90 minutes to clean the furnace and prepare for opening.

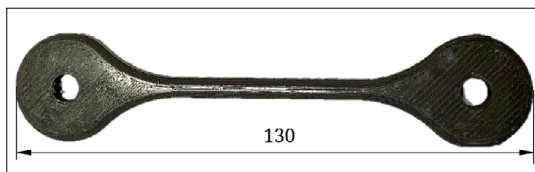


Fig. 2. The manufactured green part.

The binder removal process is illustrated in the Figure 3.

CD 3045 furnace (Figure 4) is used for removing the Catamold binder system patented by BASF.

After binder removal, sintering takes place in a different apparatus. The sintering cycle (Figure 5) begins with a re-binder removal phase. Initially, the temperature is raised to 450°C at a rate of 5°C per minute, and then held at this temperature for 150 minutes.

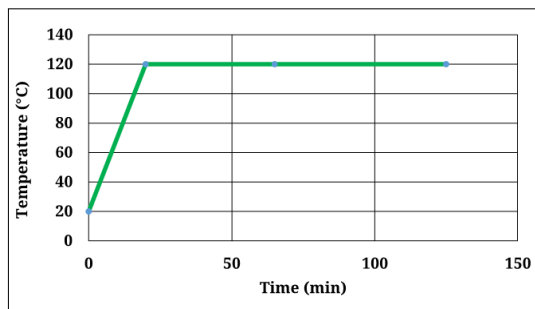


Fig. 3. Diagram of the binder removal process.



Fig. 4. CD 3045 binder removal furnace. [18]

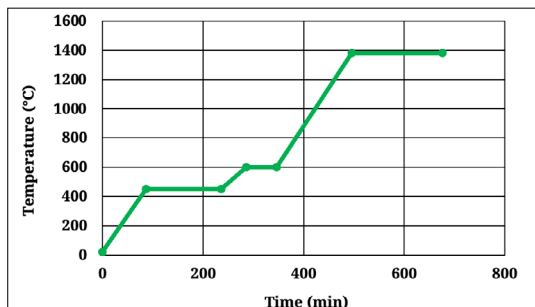


Fig. 5. Diagram of the sintering process.

The next step involves heating to 600°C at a rate of 3°C per minute and holding it for 60 minutes. Sintering occurs at 1380°C, reached at a heating rate of 5°C per minute, and held for 180 minutes. Finally, the furnace is allowed to cool freely to room temperature.

The MIM 3045 sintering furnace is shown in the **Figure 6**.

The finished specimen (**Figure 7**) with metallic properties after binder removal and sintering.

3. Results and evaluations

The following imaging techniques offer various advantages, enabling detailed analysis of the structure and composition of test specimens. The electron microscope produces high-resolution images, revealing fine details at nearly nanometer levels. The confocal microscope allows for the visualization of three-dimensional structures with optical sectioning capability. The light microscope provides a more comprehensive view of the samples, enabling observation of larger-scale features and overall morphology. These imaging methods offer valuable insights into the microstructural characteristics of the samples. The images were taken from test specimens subjected to tensile testing, which is not covered in the current research.



Fig. 6. MIM 3045 sintering furnace. [18]

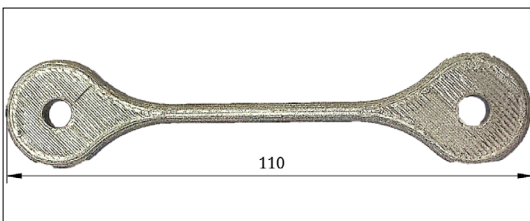


Fig. 7. The final metal specimen. [11]

3.1. Electron microscopy images

The microstructural examination images were taken using a Zeiss Sigma 300 VP scanning electron microscope (SEM) with a secondary electron (SE) detector. This detector can detect low-energy electrons, allowing for the determination of surface shape and morphology. Additionally, the backscattered electron detector (BSD) provides further assistance by identifying different elements of the periodic table with atomic number sensitivity. The images shown in **Figures 8–10** were taken from the fracture surfaces of the tensile-tested specimens.

Significant porosity is observed on the surfaces of all examined experimental samples. Porosity is influenced by the sintering conditions among other factors. An interesting phenomenon is observed on the sample of Exp. #3, where at lower magnifications, the surface of the layers appears heavily granular, yet at 2000x magnification, it seems less porous compared to the other two samples. It appears that the fusion of layers is more effective with smaller layer thicknesses.

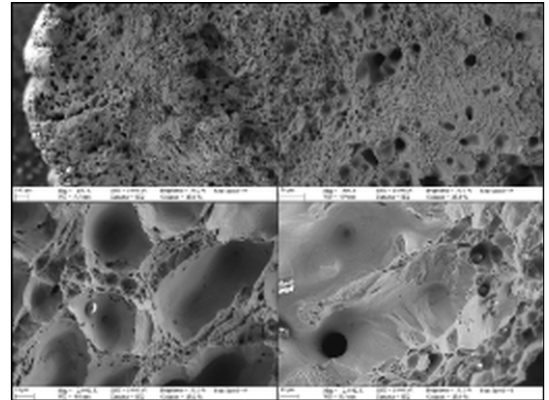


Fig. 8. Exp. #1 SEM image with SE detector.

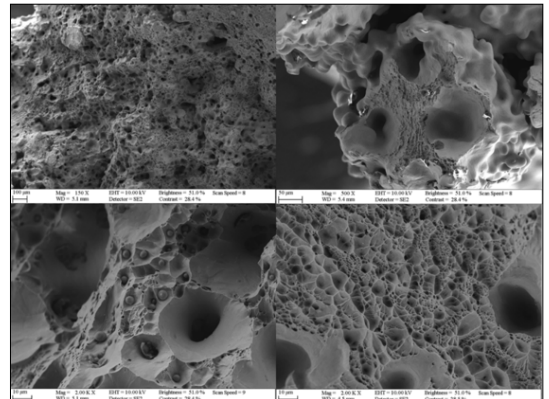


Fig. 9. Exp. #2 SEM image with SE detector.

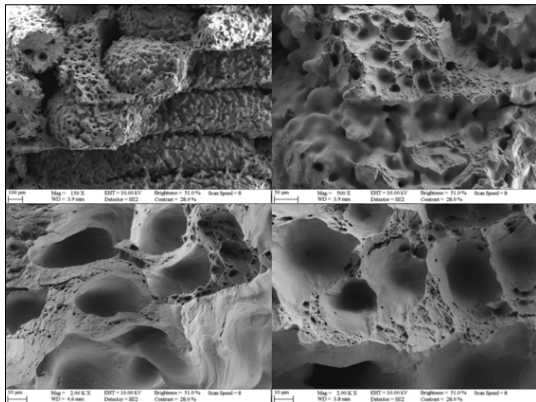


Fig. 10. Exp. #3 SEM image with SE detector.

3.2. Polished specimen sections under a light microscope

Embedded polished samples were prepared from the experiments. After polishing, the samples were analyzed using a Zeiss Axio Imager M.2m microscope. Microscopic examination allows for a comparison between the polished section and the fracture surface, with particular attention to the porosity and material continuity defects visible in the SEM images.

After polishing, images of the samples were taken. Figures 11–13. show the samples from each experiment at 25, 50 and 100× magnifications.

In Exp. #1, larger material continuity defects are observed in the initial layers, which can be attributed to the green product and, consequently, to the printing process. Although the layers mostly fused well in the inner part of the cross-section after sintering, layering is still noticeable on the outer surface (shell).

A similar observation can be made for the sample from Exp. #2, with the difference that the individual layers and weaker layer fusion are more visible in the cross-section taken from the head along the hole.

In Exp. #3, the initial layer defects are also visible, and larger material continuity defects are seen along the layers in the sample taken along the hole.

At both lower and higher magnifications, significant porosity is evident in all test specimens.

3.3. Etched and polished specimen sections under a confocal microscope

The confocal microscope creates a virtual plane through optical imaging. It can produce high-quality images with fine details and greater contrast

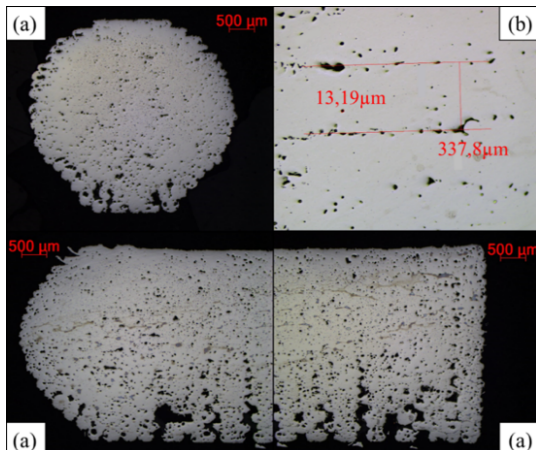


Fig. 11. Microstructural image of the Exp. #1 specimen in polished condition.

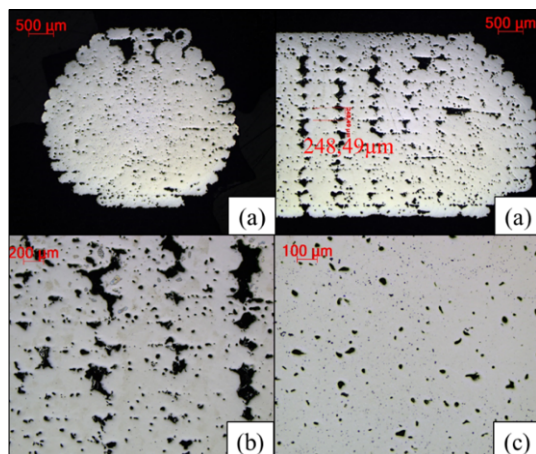


Fig. 12. Microstructural image of the Exp. #2 specimen in polished condition.

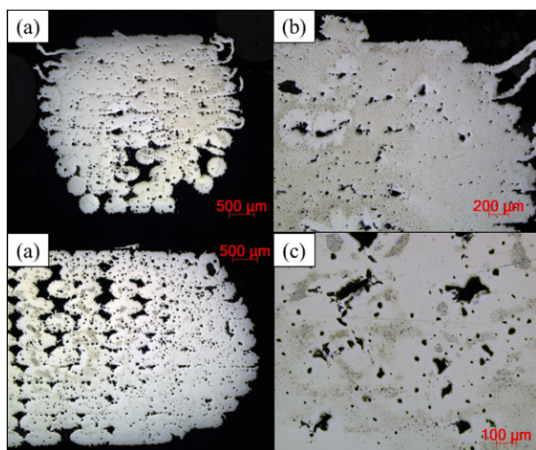


Fig. 13. Microstructural image of the Exp. #3 specimen in polished condition.

than traditional microscopes. Additionally, this imaging technique allows for the reconstruction of virtual three-dimensional images of the examined object. The microscopic images were taken using an Olympus OLS5000-SAF confocal microscope. The images captured with the confocal microscope are shown in **Figures 14–16**.

The yellowish-brown hue visible in the images is caused by the residue of the etchant remaining on the polished surface. For etching the polished sections (since the material of the sample is stainless steel) a solution called aqua regia were used, composed of:

- 10 ml nitric acid;
- 20 ml hydrochloric acid;
- 30 ml water.

The etchant was applied to the samples using a pipette, left on for 1 minute, then rinsed with water and cleaned with alcohol before drying.

The microstructures visible in the images exhibit minor variations but are generally consistent. Porosity, as observed with the light microscope, is consistently present in all experimental samples.

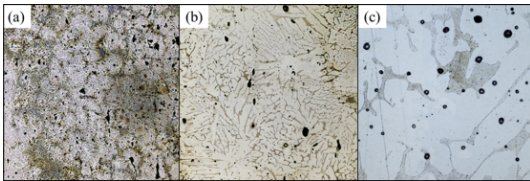


Fig. 14. Microstructural image of the Exp. #1 specimen in etched condition.

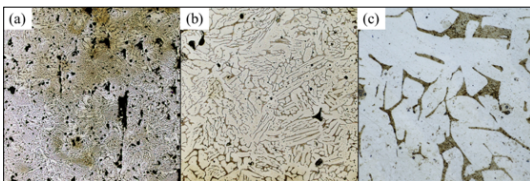


Fig. 15. Microstructural image of the Exp. #2 specimen in etched condition.

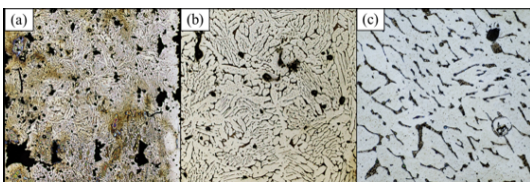


Fig. 16. Microstructural image of the Exp. #3 specimen in etched condition.

4. Conclusions

The microscopic polished samples presented in this research are part of the findings from a more extensive study. The images clearly show that the produced test specimens exhibit significant porosity. It is also observed that processing parameters have a substantial impact on the resulting micro- and macrostructure. These cavities and pores are well-visualized in the electron microscopy images. Micro- and macrostructural defects significantly reduce the achievable mechanical properties of materials produced through additive manufacturing. Therefore, defining the optimal printing strategy and parameters to achieve the best and most homogeneous products is of paramount importance. The defects identified during the research open up opportunities for further studies, such as evaluating the effectiveness of binder reduction and detailed analysis of the effects of sintering parameters.

References

- [1] Henry T. C., Morales M. A., Cole D. P., Shumeyko C. M., Riddick J. C.: *Mechanical behavior of 17-4 PH stainless steel processed by atomic diffusion additive manufacturing*. International Journal of Advanced Manufacturing Technology, 114/7–8. (2021) 2103–2114. <https://doi.org/10.1007/S00170-021-06785-1/FIGURES/13>
- [2] Nurhuda A. I., Supriadi S., Whulanza Y., Saragih A. S.: *Additive manufacturing of metallic based on extrusion process: A review*. Journal of Manufacturing Processes, 66. (2021) 228–237. <https://doi.org/10.1016/J.JMAPRO.2021.04.018>
- [3] Zhang Y., Roch A.: *Fused filament fabrication and sintering of 17-4PH stainless steel*. Manufacturing Letters, 33. (2022) 29–32. <https://doi.org/10.1016/J.MFGLET.2022.06.004>
- [4] Kedziora S., Decker T., Museyibov E., Morbach J., Hohmann S., Huwer A., Wahl M.: *Strength Properties of 316L and 17-4 PH Stainless Steel Produced with Additive Manufacturing*. Materials, 15. 15/18. 6278. <https://doi.org/10.3390/MA15186278>
- [5] Vaschetto S., Filipe J., Fernandes P., Selema A., Ibrahim M. N., Sergeant P.: *Metal Additive Manufacturing for Electrical Machines: Technology Review and Latest Advancements*. Energies 15/3. (2022) 1076. <https://doi.org/10.3390/EN15031076>
- [6] Cho Y. H., Park S. Y., Kim J. Y., Lee K. A.: *17-4PH stainless steel with excellent strength–elongation combination developed via material extrusion additive manufacturing*. Journal of Materials Research and Technology, 24. (2023) 3284–3299.
- [7] Molaei R., Fatemi A., Phan N.: *Multiaxial fatigue*

- of LB-PBF additive manufactured 17–4 PH stainless steel including the effects of surface roughness and HIP treatment and comparisons with the wrought alloy. *International Journal of Fatigue*, 137. (2020) 105646.
<https://doi.org/10.1016/j.ijfatigue.2020.105646>
- [8] Technical Datasheet 17-4 PH
https://forward-am.com/wp-content/uploads/2021/02/Ultrafuse_17-4PH_TDS_EN_v1.1.pdf (accessed on: 2024. 03. 13.)
- [9] Pellegrini A., Lavecchia F., Guerra M. G., Galantucci L. M.: *Influence of aging treatments on 17–4 PH stainless steel parts realized using material extrusion additive manufacturing technologies*. *International Journal of Advanced Manufacturing Technology*, 126/1–2. (2023) 163–178.
<https://doi.org/10.1007/S00170-023-11136-3/TABLES/6>
- [10] Nurhuda A. I., Supriadi S., Whulanza Y., Saragih A. S.: *Additive manufacturing of metallic based on extrusion process: A review*. *Journal of Manufacturing Processes*, 66. (2021) 228–237.
<https://doi.org/10.1016/j.jmapro.2021.04.018>
- [11] Sidambe A. T., Figueroa I. A., Hamilton H. G., Todd I.: *Taguchi optimization of MIM titanium sintering*. *International Journal of Powder Metallurgy*, 47/6. (2011)
<https://openurl.ebsco.com/EPDB%3Aagcd%3A6%3A13675718/detailv2?sid=ebsco%3Aplink>
- [12] Singh G., Missiaen J. M., Bouvard D., Chaix J. M.: *Additive manufacturing of 17–4 PH steel using metal injection molding feedstock: Analysis of 3D extrusion printing, debinding and sintering*. *Additive Manufacturing*, 47. (2021) 102287.
<https://doi.org/10.1016/j.addma.2021.102287>
- [13] Spiller S., Kolstad S. O., Razavi, N.: *Fabrication and characterization of 316L stainless steel components printed with material extrusion additive manufacturing*. *Procedia Structural Integrity*, 42. (2022) 1239–1248.
<https://doi.org/10.1016/j.prostr.2022.12.158>
- [14] Chemkhi M., Djouda J. M., Bouaziz M. A., Kauffmann J., Hild, F., Reira, D.: *Effects of Mechanical Post-Treatments on Additive Manufactured 17-4PH Stainless Steel Produced by Bound Powder Extrusion*. *Procedia CIRP*, 104. (2021). 957–961.
<https://doi.org/10.1016/j.procir.2021.11.161>
- [15] Liu B., Wang Y., Lin Z., & Zhang T.: *Creating metal parts by Fused Deposition Modeling and Sintering*. *Materials Letters*, 263. (2020) 127252.
<https://doi.org/10.1016/j.matlet.2019.127252>
- [16] Maj P., Adamczyk-Cieslak B., Lewczuk M., Mizera J., Kut S., Mrugala T.: *Formability, Microstructure and Mechanical Properties of Flow-Formed 17-4 PH Stainless Steel*. *Journal of Materials Engineering and Performance*, 27/12. (2018) 6435–6442.
<https://doi.org/10.1007/S11665-018-3724-9/TABLES/4>
- [17] Sadaf M., Bragaglia M., Nanni, F.: *A simple route for additive manufacturing of 316L stainless steel via Fused Filament Fabrication*. *Journal of Manufacturing Processes*, 67. (2021) 141–150.
<https://doi.org/10.1016/j.jmapro.2021.04.055>
- [18] <https://elnik.com/products/> (accessed on: 2024. 03. 13.)



Examination of the Forming Properties of Vehicle Body Panels

Richárd BORBÉLY,¹ Martin László KÖLÜS,¹ Gábor József BÉRES¹

John von Neumann University, GAMF Faculty of Engineering and Computer Science, Department of Innovative Vehicles and Materials, Kecskemét, Hungary, borbely.richard@nje.hu

Abstract

During vehicle design, the mass of the components and their resistance to collision are important criteria, as they affect fuel consumption and make the vehicle safer. In this study, we examined the deformation of high-strength materials commonly used in the automotive industry in the form of tailored welded blanks. Tests were conducted both in an experimental environment and in a simulation environment, measuring the punch displacement associated with the specimens to characterize the deformation. In designing the specimens, the weld seam was placed perpendicular and parallel to the rolling direction, thus creating different deformation states.

Keywords: *forming limit diagram, sheet metal forming, tailor welded blanks.*

1. Introduction

When designing vehicles, weight plays an important role as a criterion. By reducing weight, the fuel consumption of vehicles can be improved. Lowering fuel consumption not only makes vehicle operation more economical, but it also helps to meet increasingly stringent emission standards. It is important to note that in addition to emission requirements, numerous other equally important requirements must be considered during vehicle design, such as the collision resistance of the vehicle body, which is primarily ensured by the strength of the material. In the industry, three different methods are generally used to reduce weight. The first method is the use of high-strength, lightweight materials, known as HSS (High Strength Steel), a group of which includes dual-phase steels. These materials are characterized by excellent strength properties due to their special microstructure, allowing the required strength to be ensured with thinner sheets in specific applications. Another increasingly prevalent method today is the application of optimization techniques in structural design, such as optimizing material use or geometry based on load distribution.

The third option involves manufacturing techniques such as the use of tailor welded blanks

and various hot forming processes. Among these methods, tailor welded blanks offer significant potential for improving vehicle safety and reducing weight, which can also lower manufacturing costs through reduced tooling expenses or shorter production times. The individual parts of tailor welded blanks are tailored in size, thickness, and material quality depending on the purpose of the installation location [1, 2]. Furthermore, their application can improve the dimensional accuracy of components by potentially replacing joining processes during assembly. In this study, we analyzed the interaction of different properties of blank sections with respect to formability using the finite element method with the help of AutoFormR7 simulation software [3, 4].

2. Materials

For the selection of materials needed for the production of tailor welded blanks, we chose traditional and high-strength steels that are commonly used in the automotive industry.

2.1. Low-carbon steels

Among traditional low-carbon steels, the HC340LA cold-rolled base material was selected. The low carbon content allows for easy machinability, formability, and weldability. Thanks to cold roll-

ing, it also features good surface quality, shape, and dimensional accuracy. This type of material is mainly suitable for applications where machinability is more significant than the load-bearing capacity or strength of the finished part.

2.2. High-strength steels

Dual-phase steels are second-generation high-strength steels primarily used in the automotive industry. In these steels, the combination of soft ferrite and hard martensite components provides high strength and good formability. The characteristics of the material depend on the ferrite/martensite ratio and the distribution of martensite islands. Dual-phase steels exhibit outstanding tensile strength but do not have a distinct yield point. Martensite generally constitutes 5–30% of the microstructure, but in exceptionally high tensile strength materials, it can reach up to 40%. These materials allow for reducing damage during vehicle collisions without significantly increasing the vehicle's weight. In the test samples, HCT600X and HCT980X materials were welded separately to HC340LA material in each case.

3. Tailor-welded blanks

To conduct the tests, samples were produced in advance, which are necessary for the measurements carried out in real conditions. Tailor welded blanks consist of various properties and sizes of sheets that are joined using some welding method. These blanks present challenges in plastic forming, partly due to the presence of the weld seam. Several studies have already examined the weld seam and its surroundings to map the effects of different forming processes [5, 6].

In our case, the sheet blanks were joined using laser welding. The welding was performed without filler material, and to protect the weld seam, we used 4.6 purity argon shielding gas at a flow rate of 18 liters per minute, but only provided gas protection on the crown side. The gas was supplied by an external nozzle. In laser welding, the shape and power of the laser beam are influenced by numerous parameters, which are detailed in the MSZ EN ISO 11145 standard [7]. We selected the welding parameters based on our previous experiences, as presented in Table 1 [8]. The aim of the article is not to discuss the quality of the welding; rather, welding served the sole function of creating a solid bond between the two sheet materials. Furthermore, during the numerical analysis, the welding parameters were not utilized, as the software interprets the bonding technology differently from reality.

Table 1. Welding parameters for HC340LA-HCT600X and HC340LA-HCT980X material combinations

Pairs	HC340LA-HCT600X	HC340LA-HCT980X
Welding speed, V_h (m/min)	2.5	2.5
Continuous power output, P (kW)	1.2	1.2
Focus position (mm)	0	0
Focus spot area, A (mm ²)	0.0394	0.0394
Heat input, Q (J)	1200	1200
Power density, Q/A (W/cm ²)	$3.05 \cdot 10^6$	$3.05 \cdot 10^6$
Specific heat input, Q/v_{leg} (J/cm ²)	288	288

4. Numerical analysis

The simulation studies were conducted using the AutoFormR7 finite element software, which is one of the most advanced software tools in the field of sheet metal forming.

4.1. Tool layout

During the setup of the simulation environment, the input data was entered into the software based on realistic values. Accordingly, for determining the size and position of the tool geometries, we used a Nakazima test tool setup that can be mounted on an Erichsen 142-40 type universal sheet metal testing machine. The arrangement of forming tools and the layout of sample parts are depicted in Figures 1 and 2 within the simulation environment

In the depiction, the restraining ring is not shown, as it appears not as a geometry but as a constraint in the software. The diameter of the pull ring is 160 mm, and its iron cross-section is 15 mm. The position of the pull ring can be seen in Figure 3.

4.2. Input parameters

For achieving the most accurate simulation results, we provided the mechanical properties of the materials under investigation to correspond with reality. Therefore, from the premanufactured sample material, sheet specimens were fabricated for tensile testing, and the results of these tests were converted into input parameters.

We described the flow curves of the materials using the combined Swift-Hockett-Sherby equa-

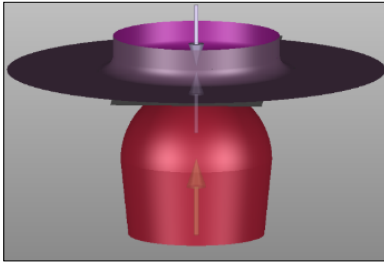


Fig. 1. Tool layout in AutoFormR7 software (side view).

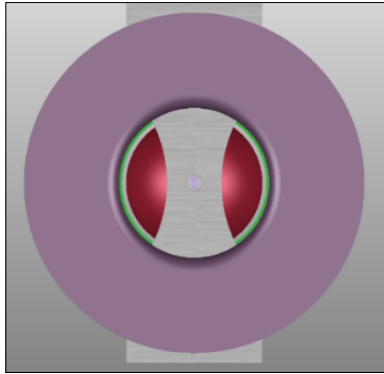


Fig. 2. Sool layout in AutoFormR7 software (top view).

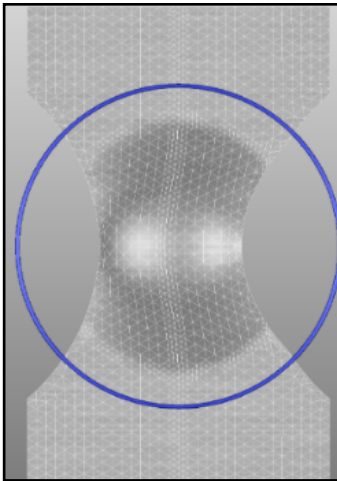


Fig. 3. The position of the pull ring (blue line).

tion [9] the input values of which are summarized in Table 2.

The parameters listed in the table are as follows: s sheet thickness, m hardening parameter, C hardening constants, σ_i true stress, σ_{sat} saturation stress, a and p weighting parameter, σ_0 initial yield stress, R_m ultimate tensile strength.

Table 2. Flow curve input data

		Material	HC 340LA	HCT 600X	HCT 980X
		s (mm)	1	1	1
Flow curve parameters	Swift	ε_0	0.02	0.04	0.01
		m	0.22	0.16	0.098
		C (MPa)	578	1044	1578
		σ_i (MPa)	229	448	788
	Hockett–Sherby	σ_{sat} (MPa)	456	780	1160
		a	8.6	21	102
		p	0.81	0.812	0.785
		σ_0 (MPa)	235	443	798.4
		R_m (MPa)	343	668.9	1122

In order to appropriately model sheet metal forming processes, it is also necessary to determine the flow stress condition. The equation describing this was also determined from tensile tests by fabricating specimens perpendicular to the rolling direction, parallel to it, and at a 45-degree angle to it. For determining the forming limit diagram, material parameters according to the Arcelor V9 model [10, 11] developed by F. Cayssials were used. The purpose of the study is not to compile and edit the forming limit diagrams of various materials. The aim of the study is to examine under identical conditions how different material pairings affect each other. The mentioned data is summarized in Table 3.

Table 3. Input data for forming limit diagram

		Material	HC340LA	HCT600X	HCT980X
Barlat' 89 model [9]	r_0	1.82	0.865	0.73	
	r_{45}	1.31	0.929	0.894	
	r_{90}	2.38	0.941	0.828	
	M	6	6	6	
	r_m	1.71	0.916	0.837	
Arcelor V9 model	$A_{G,90}$ (%)	20.5	12.5	6.3	
	$R_{m,90}$ (MPa)	325	669	1111	

The parameters listed in the table are as follows: r_0 plastic strain ratio at 0° , r_{45} plastic strain ratio at 45° , r_{90} plastic strain ratio at 90° , M weighting parameter, r_m average plastic strain ratio, $A_{G,90}$, $R_{m,90}$

4.3. The test specimens examined in the simulation

When selecting the geometry of the test specimens, in line with the tool geometries, various square specimens with different bridge widths (20-200 mm) were used, as commonly employed in Nakazima testing. The selection of test specimen geometries aimed to comprehensively cover the possible major strain regions of the forming limit diagram (FLD). Due to the different stress states created by the varied test specimen designs, the location of fracture is not constant; failure will be observed to some extent at varying locations. The utilized test specimen geometries are illustrated in **Figure 4**.

As mentioned earlier, the formation of different material pairings was done through laser welding. However, both in reality and in the simulation software, the orientation of the welding seam differed. Based on the orientation of the welding seam, two cases were distinguished: Case ‚A‘ where the welding seam (red line) is perpendicular to the rolling direction (colored line), and Case ‚B‘ where the welding seam is parallel to the rolling direction. **Figures 5** and **6** illustrate these two types on a randomly selected test specimen.

5. Simulation results

During the evaluation of the results, the basis of comparison was provided by the stamping displacement values achieved until the failure of the

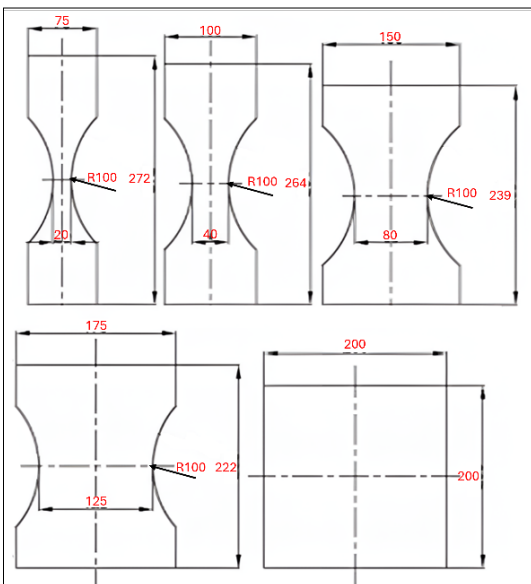


Fig. 4. Test specimen geometries

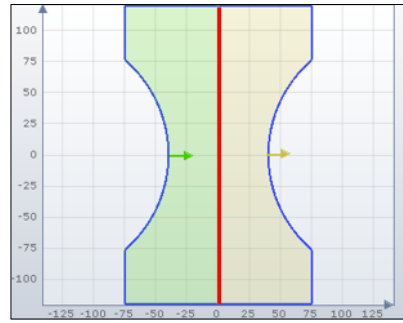


Fig. 5. Location of weld seam type ‚A‘



Fig. 6. Location of weld seam, type ‚B‘

specimens with different material pairings and welding seam orientations. The values listed in **Tables 5–8** thus illustrate the stamping displacement until failure of the specimens.

5.1. ‚A‘ type specimens

In the case of specimens with type ‚A‘ weld seams, perpendicular to the rolling direction, the evaluation of results involved continuing the forming process until one of the constituent materials reached its forming limit diagram. For the HC340LA-HCT600X material pairing, the results are summarized in **Table 4**, while for the HC340LA-HCT980X TWB, they are presented in **Table 5**. In the tables, the bridge width refers to the smallest width of the specimens.

Table 4. Material pairing of HC340LA-HCT600X with type ‚A‘ weld seam

‚A‘ type, HC340LA-HCT600X		
Bridge width (mm)	Punch stroke HC340LA (mm)	Punch stroke HCT600X (mm)
20	35.2	28.7
40	38.2	32.2
80	41.5	35.2
125	44.2	36.7
200	47.7	43.2

5. táblázat. Material pairing of HC340LA-HCT980X with type „A” weld seam

„A” type, HC340LA-HCT980X		
Bridge width (mm)	Punch stroke HC340LA (mm)	Punch stroke HCT980X (mm)
20	31.7	22.7
40	35.7	26.2
80	44.1	29.2
125	41.3	30.7
200	41.2	30.2

In this seam arrangement, except for the specimens with a bridge width of 200, the material with higher strength and simultaneously lower formability reached its forming limit diagram first. Therefore, the global formability was solely determined by the formability of the material with higher strength.

5.2. „B” type specimens

In the case of specimens with type „B” weld seams, parallel to the rolling direction, the evaluation of results involved continuing the forming process until one of the materials reached its forming limit diagram. The results are summarized in **Tables 6** and **7**.

Table 6. Material pairing of HC340LA-HCT600X with type „B” weld seam

„B” típus HC340LA-HCT600X		
Bridge width (mm)	Punch stroke HC340LA (mm)	Punch stroke HCT600X (mm)
20	31.2	–
40	34.7	–
80	31.7	–
125	30.2	–
200	34.7	38.2

Table 7. Material pairing of HC340LA-HCT980X with type „B” weld seam

„B” type, HC340LA-HCT980X		
Bridge width (mm)	Punch stroke HC340LA (mm)	Punch stroke HCT980X (mm)
20	31.2	–
40	33.7	–
80	31.2	–
125	32.7	–
200	30.2	32.2

In terms of results, it’s also important for us to know what stamping displacement a HC-340LA-HC340LA pairing yields under identical

conditions in case „B”. The results of this will be illustrated in **Table 8**.

Table 8. Material pairing of HC340LA-HC340LA with type „B” weld seam

„B” type, HC340LA-HC340LA		
Bridge width (mm)	Punch stroke HC340LA (mm)	Punch stroke HC340LA (mm)
20	36.7	36.7
40	39.6	39.6
80	44.8	44.8
125	45.8	45.8
200	54.1	54.1

From this, it can be observed that the hindering effect of deformation by the higher-strength layer significantly manifests itself on the lower-strength side, which always corresponds to the failure side in the „B” cases. Global deformation deteriorates more significantly in specimens with larger bridge widths. This can be explained by the fact that the three-axis deformation state in these specimens is reduced to a planar deformation state.

6. Conclusions

In our paper, we examined the global formability of customized welded sheets and the interaction between individual layers. The physical testing of the specimens is currently ongoing, and we primarily presented simulation results. We investigated two cases based on the orientation of the welding seam, with two different TWB configurations composed of different components, in five different deformation states each. Based on the results obtained, we can make two observations:

- In case „A”, the plates composing the specimens deformed collectively; therefore, the material with the forming limit diagram positioned lower (higher strength) experienced failure earlier, with the exception of the 200x200 mm case;
- In case „B”, the lower strength material (HC-340LA) consistently fails earlier. Furthermore, it can be noted that the failure point is significantly unaffected by the different strength materials (HCT600X-HCT980X) within this strength range.

As part of the research, our further aim is to investigate material pairings where the HC340LA material is paired with other materials of varying strength levels, in order to observe the effect of strength differences on global formability. Addi-

tionally, we will conduct tests on existing specimens in real-world conditions, following the method outlined in the simulation environment, and compare their results with the simulation findings.

References

- [1] Kinsey B., Wu X. (szerk.): *Tailor welded blanks for advanced manufacturing*. Elsevier, Cambridge, 2011. 95–115.
- [2] Safdarian R.: *Forming limit diagram prediction of tailor welded blank by modified M-K model*. Mech. Res. Commun., 67. (2015) 47–57.
<https://doi.org/10.1016/j.mechrescom.2015.05.004>
- [3] Korouyeh R. S., Naeini H. M., Liaghat G. H., Kasaei M. M.: *Investigation of weld line movement in tailor welded blank forming*. In: *Advanced Materials Research*, Trans Tech Publications Ltd., 2012. 39–44.
<https://doi.org/10.4028/scientific5/AMR.445.39>
- [4] Safdarian R.: *The effects of strength ratio on the forming limit diagram of tailor-welded blanks*. Ironmaking Steelmaking, 45/1. (2018) 17–24.
<https://doi.org/10.1080/03019233.2016.1235371>
- [5] Merklein M., Johannes M., Lechner M., Kuppert A.: *A review on tailored blanks – Production, applications and evaluation*. Journal of Material Processing Technology, 214/2. (2014) 151–164.
<https://doi.org/10.1016/j.jmatprotec.2013.08.015>
- [6] Ahmetoglu M. A., Brouwres D., Shulkin L., Taupin L., Kinzel G. L., Altan T.: *Deep drawing of round cups from tailor-welded blanks*. Journal of Material Processing Technology, 53/3-4. (1995) 684–696.
[https://doi.org/10.1016/0924-0136\(94\)01767-U](https://doi.org/10.1016/0924-0136(94)01767-U)
- [7] Béres G. J., Danyi J. Végvári F., Tisza M.: *The present body in white materials*. Gradus, 2/2. (2015) 209–224.
- [8] Kovács Zs. F., Béres G., Weltsch Z.: *The Investigation of DC and DP steels weldability by laser beam*. Gradus, 4/2. (2017) 311–317 .
- [9] Barlat F., Lian K.: *Plastic behavior and stretchability of sheet metals. Part I: A yield function for orthotropic sheets under plane stress conditions*. International Journal of Plasticity, 5/1. (1989) 51–66.
[https://doi.org/10.1016/0749-6419\(89\)90019-3](https://doi.org/10.1016/0749-6419(89)90019-3)
- [10] Cayssials F.: *Sheet Metal Forming Beyond 2000*. Proc. of the 20th Biennial [IDDRG] Congress, Brussels, Belgium (Liege: CRM), 1998. 443–54.
- [11] Cayssials F., Lemoine X.: *Proc. of the 24th IDDRG Congress*. Besancon, France, 2005. 1–8.



Corrosion Testing of Laser Welded Austenitic Stainless Steel Welds

Csaba BREZNAY,¹ Balázs VARBAI²

¹ *Budapest University of Technology and Economics, Faculty of Mechanical Engineering, Department of Materials Science and Engineering, Budapest, Hungary, breznay.csaba@edu.bme.hu*

² *Budapest University of Technology and Economics, Faculty of Mechanical Engineering, Department of Materials Science and Engineering, Budapest, Hungary, varbai.balazs@gpk.bme.hu*

Abstract

Laser welding is becoming increasingly common in industrial applications for welding stainless steels. To reduce costs, hot-rolled stainless steel beams can be replaced by laser-welded structures. In our research, the corrosion resistance of laser-welded T-joints made of 1.4301/304 austenitic stainless steel were investigated. The joints were welded one or both sides, with different combinations of travel speed and laser power. Electrochemical corrosion measurements were performed in 3.5% NaCl solution in a standard three-electrode corrosion cell.

Keywords: *laser welding, stainless steel, electrochemical corrosion.*

1. Introduction

Laser welding (52 according to ISO 4063:2023) is becoming increasingly common in industrial applications. Thanks to the high energy density, welding can be performed with lower heat input, low heat-affected area and higher productivity (travel speed) [1, 2]. Due to the low thermal conductivity of stainless steels, there is a significant amount of warping during welding, which can be reduced by the low heat input of laser welding. In laser welding, a distinction is made between solid-state laser welding, gas laser welding and diode laser welding. Thanks to the rapid development of the technology, a fusion depth of up to 15 mm can be achieved when welding stainless steels [3, 4].

Stainless steels are steels containing at least 10.5% chromium and up to 1.2% carbon [5]. Thanks to chromium alloying, a passive oxide layer is formed on their surface, which protects them from environmental effects. Rolled and welded stainless steel beams are increasingly used in structural engineering and interior design. Thanks to their corrosion resistance, maintenance tasks can be reduced. The most commonly used material grades are 1.4301 (AISI 304) and 1.4404 (AISI 316L) austenitic stainless steels [6, 7].

Corrosion is the physico-chemical interaction between a metal and its environment, which results in a change in the properties of the metal and often in a deterioration of the functional properties of the metal, the environment and the engineering system they form [8]. The typical mode of failure for stainless steels is some form of localised corrosion attack. The most common form of localised corrosion is pitting. This form of corrosion is a localised anodic dissolution concentrated in a small area, the rate of which can be extremely rapid. It occurs in the form of pits or holes on the surface, with varying morphologies and depths.

The corrosion resistance of nickel alloys and stainless steels can be determined from their composition by the pitting resistance equivalent (PRE). The most commonly used method for austenitic and duplex steels are:

$$\text{PREN} = \text{Cr} + 3.3 \cdot \text{Mo} + 16 \cdot \text{N}$$

Electrochemical corrosion measurements can be used to determine the pitting corrosion potential of materials with a passive layer, at which voltage the surface passive layer is locally damaged and the metal goes into solution.

2. Test materials and methods

In our research, we used austenitic corrosion resistant steel material grade 1.4301 (AISI 304) with a thickness of 4 mm, the composition of which is shown in [Table 1](#).

The T-joints were made without chamfering and without a joint gap using tack welds.

Table 1. The chemical composition of material grade 1.4301

Symbol	C	Mn	Si	Cr	Ni
1.4301	0.08	2	0.75	18	8

The welds were made with two WSX ND60 welding heads powered by a Raycus RFL-6600S laser source with a nominal power of 6600 W. The two side T-joints were made simultaneously with two fillet welds using two laser welding heads facing each other.

The welds were made with three different parameter combinations: the samples welded from both sides ([Figures 1 and 2](#)) at 1.5 m/min with a power of 3630 W and at 2 m/min with a power of 4620 W.

The sample welded from one side ([Figure 3](#)) was produced at a speed of 1 m/min and a power of 3960 W.

The laser beam was wobbled along a straight line 0.2 mm wide for each sample. The shielding gas used for welding was grade 4.6 nitrogen.

Electrochemical corrosion measurements were carried out using a standard three-electrode corrosion cell and a Biologic SP-150 potentiostat. The test setup is shown in [Figure 4](#): a platinum mesh was used as a counter electrode, an oversaturated AgCl/KCl electrode as a reference electrode and the welded sample as the working electrode. The electrolyte was a 3,5 % NaCl solution prepared from high purity NaCl and distilled water.

After the corrosion cell was assembled, the system was left to rest for 45 min to stabilize the open circuit potential (OCP). After resting, the voltage was scanned from OCP = -0.2 V to OCP = +1.5 V at a rate of 1 mV/s.

3. Results and discussion

The current density–potential curves recorded by the potentiostat were used to compare the corrosion properties of each joint [Figure 5](#) shows the results of the three test specimens.

The open circuit potentials of the samples are shown in [Table 2](#). The open circuit potential of the hot-rolled plate is -0.07 ± 0.02 V. The open cir-

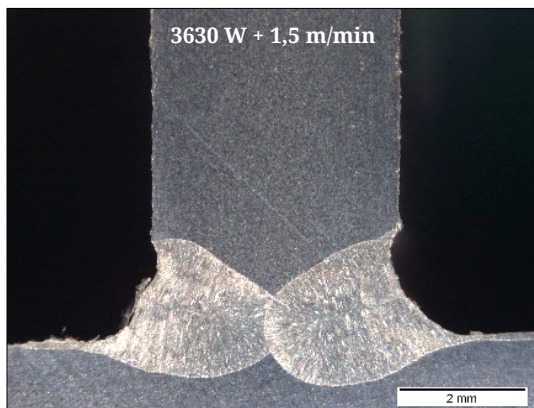


Fig. 1. Cross section of the two sided T-joint, etched with Adler

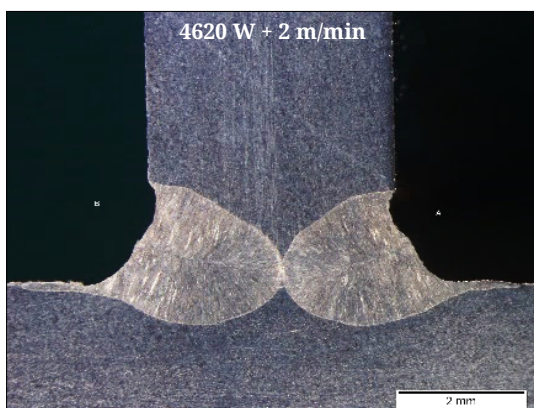


Fig. 2. Cross section of the two sided T-joint, etched with Adler.

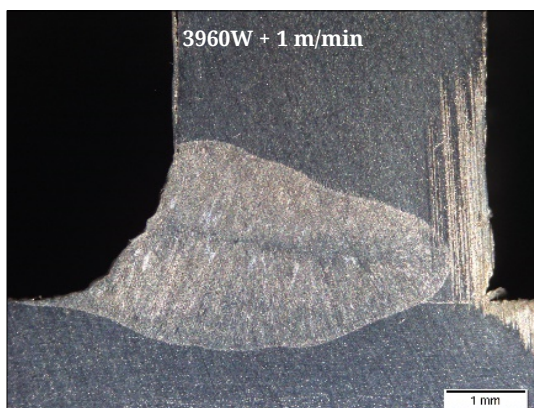


Fig. 3. Cross section of the one sided T-joint, etched with Adler.

cuit potential of the three welded samples is almost the same, no significant difference can be measured between the samples.

Table 2. The open circuit potentials of the samples measured in 3,5% NaCl solution

Sample	OCP
3630 W + 1.5 m/min	-0.11 ± 0.02 V
4620 W + 2 m/min	-0.11 ± 0.03 V
3960 W + 1 m/min	-0.10 ± 0.03 V

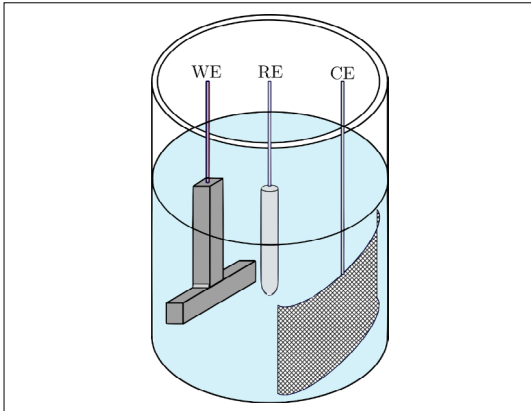


Fig. 4. Standard three electrode corrosion cell setup.

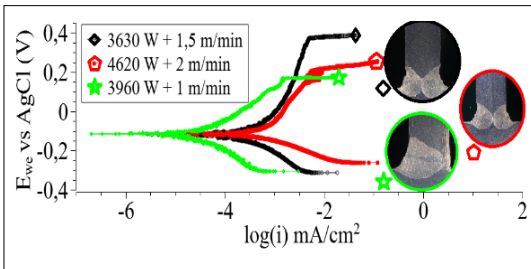


Fig. 5. The results of the electrochemical corrosion measurements conducted in 3,5% NaCl solution.

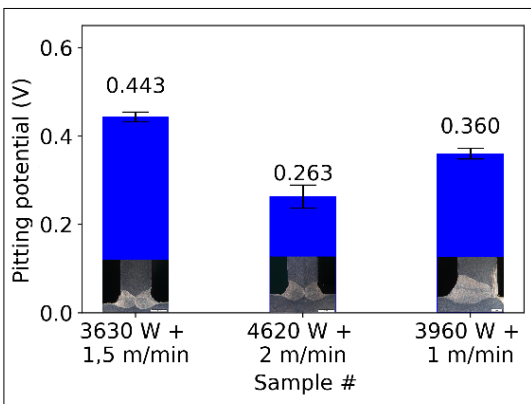


Fig. 6. The pitting potentials of the samples, measured in 3,5% NaCl solution.

The curves shown in **Figure 5** can be divided into three distinct parts: the initial reduction phase, the oxidation phase during the scanning of voltages more positive than the open circuit potential, and the subsequent passive phase. During the passive phase, the current density does not increase, or increases only very slightly, as the voltage increases. When the voltage is increased beyond a certain point, the current density increases rapidly, this voltage is called the pitting potential.

The T-joint welded from both sides at a travel speed of 1.5 m/min shows the highest pitting potential. The pitting potential of each sample is shown in **Figure 6**.

The more negative the pitting potential of a given sample in a given medium, the sooner and easier it is for pitting to occur. A more positive pitting corrosion potential indicates a more noble behaviour and better corrosion properties in the given medium.

4. Conclusions

In our study, we investigated the corrosion properties of single- and double-sided T-joints prepared by laser welding at different power and different travel speeds in a 3.5% NaCl solution. Based on the obtained current density–potential curves, the specimen welded at a speed of 1.5 m/min and a power of 3630 W showed the highest pitting potential. The pitting potential of the sample also welded from both sides at 2 m/min with a power of 4620 W was significantly lower, presumably due to excessive undercut.

The T-joint, made from one side with a power of 3960 W and a travel speed of 1 m/min, was not a full penetration weld, which is likely to have caused crevice corrosion in the joint gap, resulting in increased current density and lowering the measured pitting potential. To confirm this hypothesis, it is necessary to examine the site of pitting corrosion in the welded joint.

Acknowledgements

The publication was funded by the National Research, Development and Innovation Office - NKFIH (OTKA PD 138729).

References

[1] Landowski M., Świerczyńska A., Rogalski G., Fydrych D.: *Autogenous Fiber Laser Welding of 316L Austenitic and 2304 Lean Duplex Stainless Steels*. Materials, 13/13. (2020) 2930. <https://doi.org/10.3390/ma13132930>

- [2] Landowski M.: *Influence of Parameters of Laser Beam Welding on Structure of 2205 Duplex Stainless Steel*. *Advances in Materials Science*, 19/1. (2019) 21–31.
<https://doi.org/10.2478/adms-2019-0002>
- [3] Alcock, J. A., Baufeld, B.: *Diode laser welding of stainless steel 304L*. *Journal of Materials Processing Technology*, 240. (2017) 138–144.
<https://doi.org/10.1016/j.jmatprotec.2016.09.019>
- [4] Hafez K. M., Katayama S.: *Fiber laser welding of AISI 304 stainless steel plates*. *Quarterly journal of the japan welding society*, 27/2. (2009) 69s–73s.
- [5] MSZ EN ISO 10088-1: *Korrózióálló acélok*. 1. rész: A korrózióálló acélok jegyzéke. 2015.
- [6] Outokumpu: *Handbook of Stainless Steel*. 2014.
- [7] Ran H., Chen Z., Ma Y., O'Brien E., Sun Y.: *Experimental and numerical study of laser-welded stainless steel slender I-section beam-columns*. *Engineering Structures*, 286. (2023) 116–128.
<https://doi.org/10.1016/j.engstruct.2023.116128>
- [8] MSZ EN ISO 8044:2003 *Fémek és ötvözetek korróziója*. Alapvető szakkifejezések és fogalom meghatározások (ISO 8044:1999).



Investigation of Microhardness of Multiaxially Forged Copper Samples

Zsombor JUHÁSZ,¹ József Bálint RENKÓ²

¹ Budapest University of Technology and Economics, Faculty of Mechanical Engineering, Department of Materials Science and Engineering, Budapest, Hungary, zsombor.juhasz@edu.bme.hu

² Budapest University of Technology and Economics, Faculty of Mechanical Engineering, Department of Materials Science and Engineering, Budapest, Hungary, renko.jozsef@edu.bme.hu

Abstract

In engineering practice, high strength materials attract extraordinary attention. Such materials can be produced by many different methods, from which, multiaxial forging was selected. In this work a sum of four samples were compressed by two-directional multiaxial forging. The achieved logarithmic deformation in each step was 0.8 while the accumulative plastic strain of the workpieces were 0.8, 1.6, 2.4, and 3.2. The hardness of the samples was examined in 200 points of measurement on the surface of the mid-section of each to investigate hardening patterns.

Keywords: *severe plastic deformation, multiaxial forging, microstructural analysis.*

1. Introduction

The methods of severe plastic deformation (SPD) are especially suitable for enhancing strength, toughness, and fatigue resistance [1, 2]. During SPD, due to the high amount of plastic deformation, an increase in dislocation density will be apparent. This causes an increase in areas surrounded by non-equilibrium grain boundaries. These are the so-called dislocation cells. The emerging structure can be nano (NG) or ultrafine (UFG) grained. The former is made of dislocation cells, where grains differ from each other only by a couple of degrees in their orientation [3, 4], while in the latter, grains are bound by high-angle equilibrium boundaries. These “building blocks” are formed as the dislocation density rises and the borderline dislocations eliminate each other. Differences show in the size as well. The nano-grained area is defined on an interval between 10-100 nm, while the UFG territory starts at couple hundred nm and ends at 1 μm [3, 5].

When using the methods of SPD, the aim usually is the creation of UFG structure. Former studies showed that materials, that possess such a structure would be able to endure much higher defor-

mation compared to common, cold rolled steel, along the grain refinement induced increase in strength [6, 7].

When examining the UFG and coarse-grained variation of the same material, UFG will be able to deform almost as much as the latter, while its strength could exceed several times that of the cold rolled state [7].

Though SPD includes several processes this study focuses primarily on multiaxial forging [8].

As a result of our previous research, a closed-die multiaxial forging tool, capable of producing UFG structure, was manufactured [9]. Microstructural examinations were conducted on workpieces formed by this tool in the transverse and normal directions. These showed the formation of UFG structure, along with a higher hardness in the middle line of the samples defining a characteristic pattern for each one of them. When moving towards the side of the sample, the increase in hardness shows a declining gradient. This difference is caused by the design of the tool. The sides of the samples that show a lower hardness contact the covers of the die, which resulted in friction hindered deformation despite good lubrication [10].

Our aim with this study was to expand previous findings by examining the longitudinal section of workpieces processed by the same tool on the same deformation spectrum.

2. Experimental

2.1. Material

The material used for the experiments was Cu99.9 industrial grade copper. The material was already at our disposal due to former studies, and the dimensions of the tool were determined so that they could withstand the resulting forces from the sample during the process.

A total of 4 column-shaped workpieces were produced of the chosen material. These had the nominal dimensions of 10×10×20 mm. After manufacturing, the pieces were subjected to heat treatment for 15 minutes at 950 °C, then cooled in water.

2.2. Equipment

A sketch of the closed-die multi-axial forging tool is shown in **Figure 1**. The tool can be divided into three main parts. These are the center block, the tool housing, and the linear actuators. The first one is responsible for positioning the stamps, furthermore it is connected through an intermediate piece to the housing. The latter is to provide a frame embracing the tool, as well as to aid in the tool movements. The main function of the linear actuators is to move the stamps and forward the load to them.

The forming done by the tool is shown in **Figure 2**. It is important to highlight that at any step, only one of the two pairs of stamps is working, while the other is always secured in its position, passively closing die (**Figure 2a**). When finishing a forging step (**Figure 2b**), the ejectors are pushed in, settling back to the initial positioning (**Figure 2c**). Following this, another forging step can be executed, concluding a whole forging cycle (**Figure 2d**).

2.3. Experiment

The forming of the workpieces was done with an MTS 810 type universal material testing machine. The performed forming cycles of the samples were 0.5, 1, 1.5 and 2, respectively. Due to the design of the tool, each forging step caused 0.8 logarithmic plastic deformation. Hence, the cumulative plastic strain was 0.8, 1.6, 2.4 and 3.2, respectively.

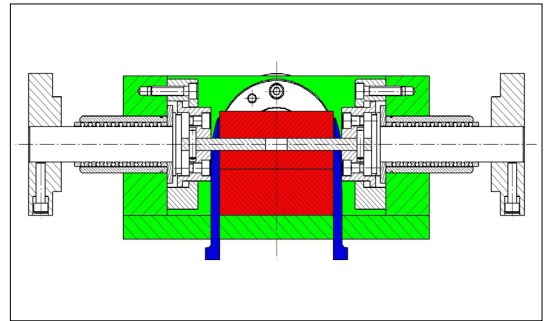


Fig. 1. Sketch of the multi-axial forging tool. The color markings are as follows: the center block is red, the housing is green, and the ejectors are blue. Uncolored parts (excluding the screws) belong to the linear actuators.

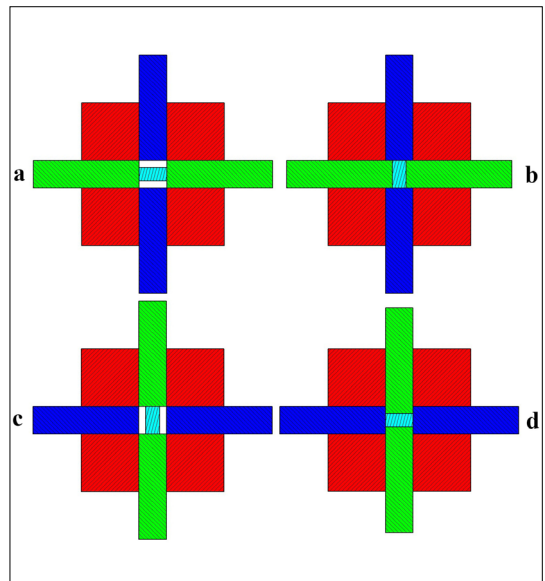


Fig. 2. Demonstration of one forging cycle. Red shows the housing that positions stamps, the active stamps are blue, while the passive ones are green. The workpiece is turquoise.

First, as preparation for the metallographic examination, the workpieces were cut on the longitudinal 10×20 mm cross-section along the centerline, parallel to the sides, which came in contact with the covers of the die. The cutting was followed by grinding and polishing. Both steps were performed on a Struers Tegramin-30 type automatic polishing machine. In the last polishing step 1 μm diamond suspension was used with 10 N load on each sample for 8 min.

2.4. Microhardness testing

After the preparation of the samples, microhardness was measured on their surfaces at 200 points. The examination was extended with a virgin (non-deformed) sample for reference. In this case, however, the measurement was performed at only 40 points due to the assumption of isotropic microstructure. The matrix of the measurement points is shown in **Figure 3**. One is for the non-formed sample (a), while the other is for the formed workpieces (b). The outer points of the matrix are 0.5 mm from the edge of both specimens, thus, in the latter case, some points may fall into the resin. These, however, can be easily distinguished since there is a significant difference in the hardness of the resin and the copper.

The measurements were completed using an MCT type programmable microhardness test instrument. This uses the Oliver & Pharr (O&P) method [11] for the calculation of hardness, based on the indentation and the load of the piercing tool.

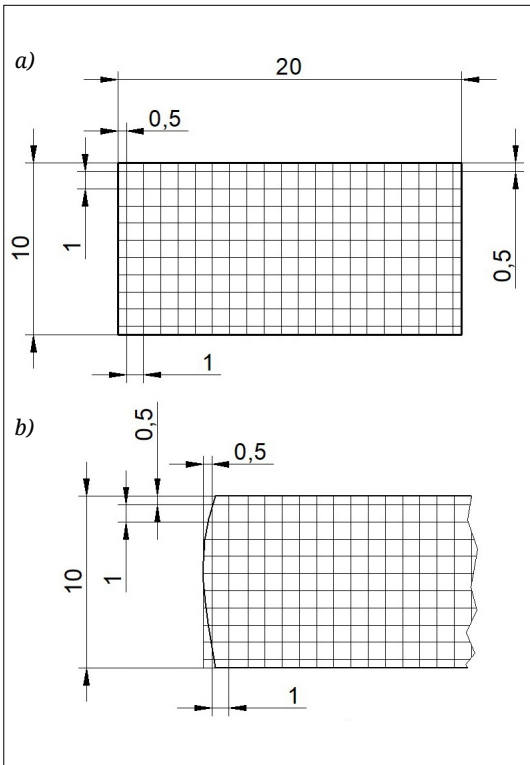


Fig. 3. Measurement matrix on the virgin (a) and the formed (b) specimens. Every intersection indicates a measurement point.

3. Results

Based on the measured points, the hardness map of each sample was generated as seen in **Figures 4–8**. The missing points on the maps were artifacts, mostly indented into the resin. The range of the scales was defined globally, so that the different maps could be compared to one another. On the left side of each scale the minimal and maximal hardness value of the measurement belonging to that specific map is presented.

Figure 4 shows that the hardness map is homogeneous, the hardness values on the virgin sample are between 32–65 HV0,5 (avg: 52.6±8,3 HV0,5). This interval is sufficiently narrow, thus, the 40 measurement points are sufficient to represent the hardness of the whole surface. Furthermore, since all the specimens were prepared the same way, their initial state can be assumed isotropic.

The most significant increase in hardness occurred right after the first forging step (**Figure 5**). Although only faintly visible, the characteristic pattern (later visible for each sample) appears as well: a much higher hardness can be observed along the diagonals [12]. The microhardness here appears between 102.3–177.3 HV0,5.

By the end of the first forming cycle (**Figure 6**) By the end of the first forming cycle.

In the third forming step the interval of the values of hardness narrows down between 124.4–189.6 HV0,5 (**Figure 7**), which indicates a conspicuous rise in hardness on the edges of the specimen. At the same time the widening of the middle, high hardness territory can be observed. This is caused by the hardening of the parts that deform to a higher extent, and therefore, are

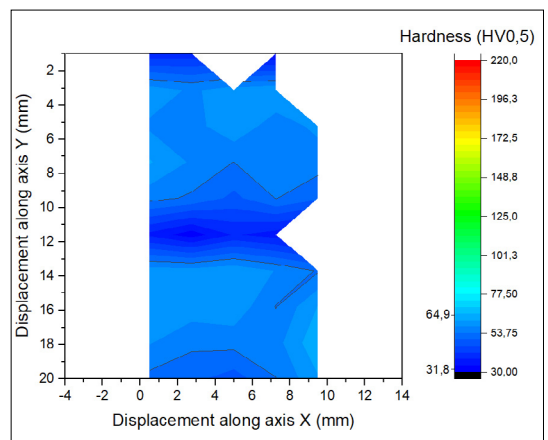


Fig. 4. Hardness map of the reference specimen.

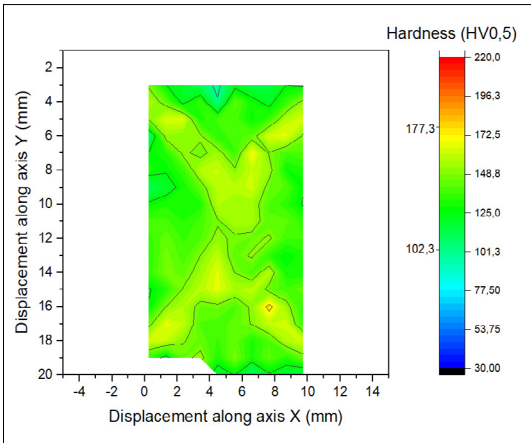


Fig. 5. Hardness map of the specimen formed for one step.

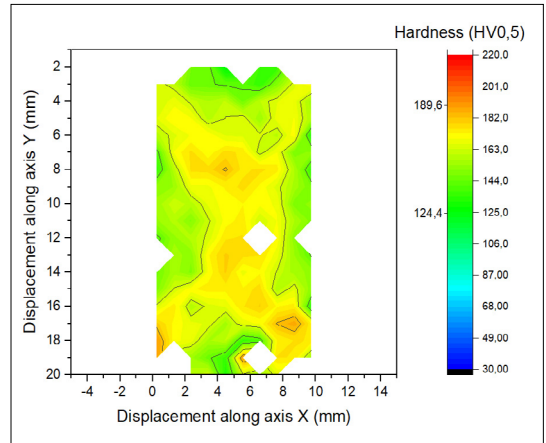


Fig. 7. Hardness map of the specimen formed for three steps.

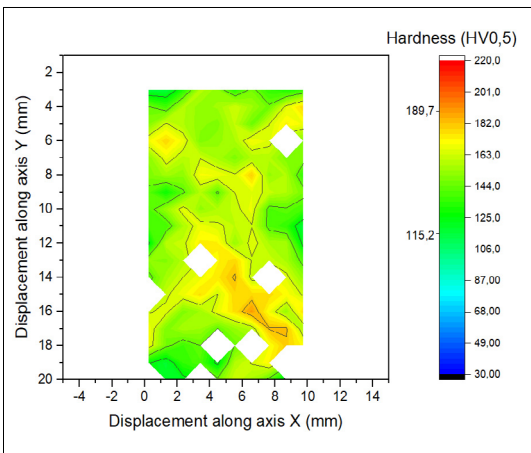


Fig. 6. Hardness map of the specimen formed for one cycle.

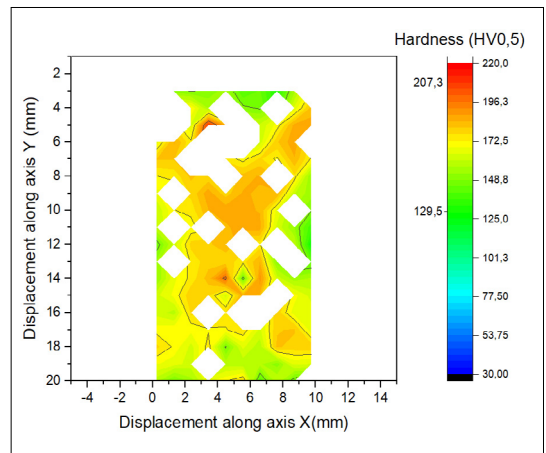


Fig. 8. Hardness map of the specimen formed for two cycles.

more resistant to deformation, causing the less deformed parts to gain in on them.

By the end of the second forming cycle (**Figure 8**), the hardness-interval is pushed and narrowed down. Thus, the hardness values will be between 129.5–207.3 HV0,5. This phenomenon can be experienced in comparison with the third forming step along the diagonals as well. On the edges of the specimen a low hardness zone is separated.

Figures 9–12 show the distribution of the hardness for different steps. Until the third forming step the histograms show a movement in the direction of the higher hardness. By the second forming cycle, the peak stays between 170 HV0,5 and 180 HV0,5, though the interval of distribution

narrows down and does not lie as wide as in the third step.

4. Conclusions

It was made clear, that using the O&P method causes significantly more errors to appear than with the use of a manual hardness measuring method. Nonetheless the productivity of this method compensates for the number of errors, for in the time needed to complete the manual examination, several times as many measurements can be completed with the O&P method.

The characteristic cross-shaped pattern along the diagonals is formed because of the friction between the workpiece and the die, despite good lubrication. The friction causes the workpiece at

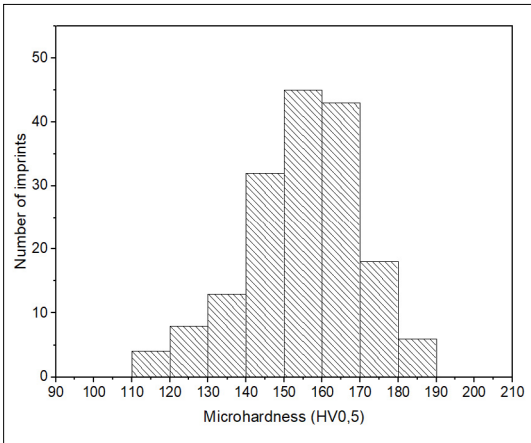


Fig. 9. The histogram of the hardness values of the first forming step.

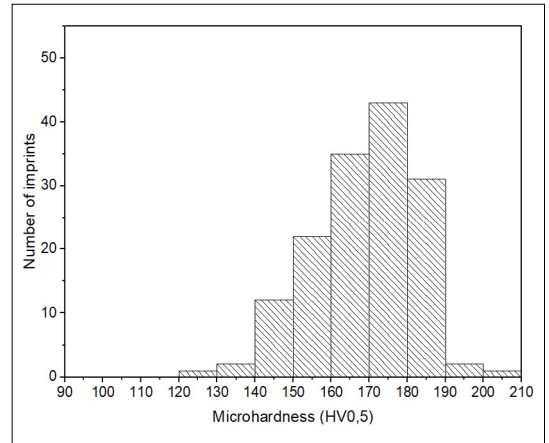


Fig. 11. The histogram of the hardness values of the third forming step.

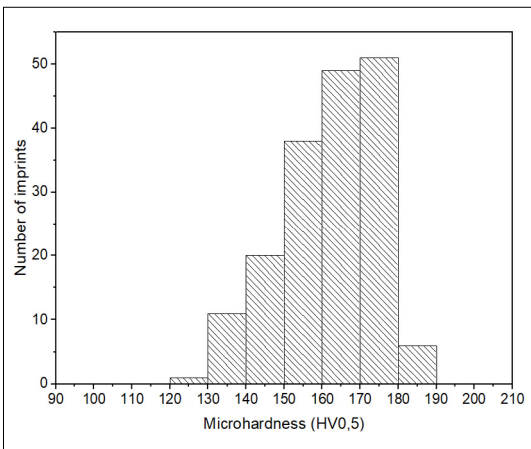


Fig. 10. The histogram of the hardness values of the first forming cycle.

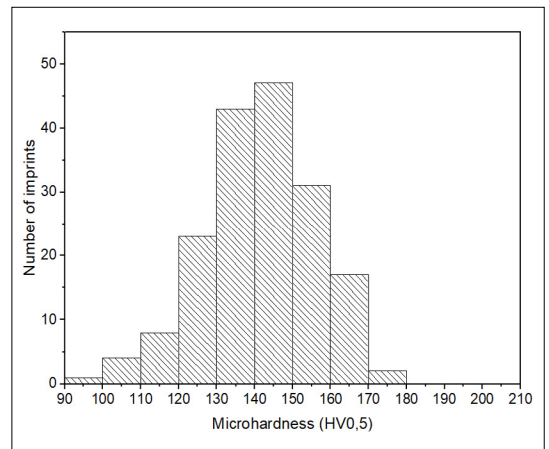


Fig. 12. The histogram of the hardness values of the second forming cycle.

these contact areas to stick to the covers, thus reducing the deformation they suffer in these areas, and at the same time inflicting more significant deformation along the diagonals.

Based on **Figures 9–12** the following statement can be made: until the end of the second forming cycle, the hardness rises continuously. This is illustrated through the displacement of the histograms.

Acknowledgement

Supported by the ÚNKP-23-2-I-BME-372 New National Excellence Program of the Ministry for Culture and Innovation from the source of the National Research, Development and Innovation Fund. The Department of Materials Science and Engineering and the Department of Automotive Technologies

of Budapest University of Technology and Economics deserves our special gratitude for providing us the lab equipment necessary for our research, as well as the Institute of Machine Tools and Mechatronics of the University of Miskolc for granting the space and equipment necessary to operate the tool.

References

- [1] Langdon T. G.: *The principles of grain refinement in equal-channel angular pressing*. Materials Science and Engineering A, 462/1–2. (2007) 3–11. <https://doi.org/10.1016/j.msea.2006.02.473>
- [2] Huang Y., Langdon T. G.: *Advances in ultrafine-grained materials*. Materials Today, 16/3. (2013) 85–93. <https://doi.org/10.1016/j.mattod.2013.03.004>
- [3] Siegel R. W.: *Nanophase Materials*. 11. kiadás. VCH Publishers, 1994.

- [4] Mughrabi H.: *Dislocation wall and cell structures and long-range internal stresses in deformed metal crystals*. Acta Metallurgica, 31/9. (1983) 1367–1379.
[https://doi.org/10.1016/0001-6160\(83\)90007-X](https://doi.org/10.1016/0001-6160(83)90007-X)
- [5] Chang C. P., Sun P. L., Kao P. W.: *Deformation induced grain boundaries in commercially pure aluminium*. Acta Materialia, 48/13. (2000) 3377–3385.
[https://doi.org/10.1016/S1359-6454\(00\)00138-5](https://doi.org/10.1016/S1359-6454(00)00138-5)
- [6] Bereczki P. et al: *Production of ultrafine grained aluminum by cyclic severe plastic deformation at ambient temperature*. In: Institute of Physics, Franciaország, Conf. Ser.: 6th International Conference on Nanomaterials by Severe Plastic Deformation. (2014) 1–11.
<https://doi.org/10.1088/1757-899X/63/1/012140>
- [7] Valiev R. Z.: *Bulk nanostructured materials from severe plastic deformation*. Progress in Materials Science, 45/2. (2000) 103–189.
[https://doi.org/10.1016/S0079-6425\(99\)00007-9](https://doi.org/10.1016/S0079-6425(99)00007-9)
- [8] Sakai T., et al.: *Dynamic and post-dynamic recrystallization under hot, cold and severe plastic deformation conditions*. Progress in Materials Science, 60. (2014) 130–207.
<https://doi.org/10.1016/j.pmatsci.2013.09.002>
- [9] Juhász Zs, Bíró T., Renkó J. B.: *Design and Manufacture of closed die multiaxial forging tool*. In: Institute of Physics, Hungary, Conf. Ser.: Mater. Sci. Eng. 1246. (2022) 1–7.
<https://doi.org/10.1088/1757-899X/1246/1/012009>
- [10] Juhász Zs.: *Zárt üregű többtengelyű kovácsolással alakított réz próbatestek mikroszerkezeti vizsgálata*. Szakdolgozat. BME Anyagtudomány és Technológia Tanszék 2022.
- [11] Oliver W. C., Pharr G. M.: *Measurement of hardness and elastic modulus by instrumented indentation: Advances in understanding and refinements to methodology*. Journal of Materials Research, 19. (2003) 3–20.
<https://doi.org/10.1557/jmr.2004.19.1.3>
- [12] Juhász Zs.: *A többtengelyű kovácsolás mikroszerkezeti hatásainak vizsgálata*. TDK-article. BME Department of Materials Science and Engineering, Budapest, 2022.



Effect of the Slenderness Relation on In-Plane Deformation in Stack Compression Tests

Martin László KÖLÜS,¹ Richárd BORBÉLY,² Gábor József BÉRES³

¹ John von Neumann University, GAMF Faculty of Engineering and Computer Science, Department of Innovative Vehicles and Materials, Kecskemét, Hungary, kolus.martin@nje.hu

² John von Neumann University, GAMF Faculty of Engineering and Computer Science, Department of Innovative Vehicles and Materials, Kecskemét, Hungary, borbely.richard@nje.hu

³ John von Neumann University, GAMF Faculty of Engineering and Computer Science, Department of Innovative Vehicles and Materials, Kecskemét, Hungary, beres.gabor@nje.hu

Abstract

In forming technologies and their simulation, knowing the flow curve characteristic of the material is an essential parameter. Acquiring this knowledge is particularly challenging for sheet materials in high strain ranges. It is well-known that friction and geometric relationships have a distorting effect on the flow curves, thus compensation is necessary. However, the geometric ratio can not only influence the formation of the flow curve, if our material shows anisotropic behaviour. In our research, using compression tests, we examined the deformation relations of deformed specimens through digital imaging methods. The stack compression test is widely used to determine the flow curve in a broad range of large deformation. During the test, several disk specimens with the same geometric characteristics were stacked on top of each other to form a final test piece, and then compression tests were conducted on these assemblies. We found that at low values of the geometric ratio (0.1 in our study), the proportion of plastic, planar principal strains indicating anisotropic behaviour is greater than at higher geometric ratios (0.5 and 1.0 in our study).

Keywords: *disk compression test, stack compression test, anisotropy.*

1. Introduction

The stack compression tests are mentioned in early literature with the aim of extending the measurable range of material behaviour to include larger deformations beyond those covered in tensile tests. Additionally, Barlat et al. [1] proposed describing the biaxial material behaviour with the normal direction compression of sheets.

Accurate knowledge of flow curves is essential for various sheet forming technologies. Understanding higher deformation ranges, which are often encountered during sheet forming, poses significant challenges. To gain insight into these ranges, several methods have been developed, such as uniaxial compression testing, hydraulic bulge testing, the Watts–Ford-test, or the stack compression test [2]. Merklein and Kuppert [3] were among the first to conduct stack compression test, which we also employ in our study.

While each method has its advantages and disadvantages, friction and geometric considerations are particularly troublesome in methods involving methodology of compression. Regarding friction, it is commonly assumed to be constant during testing, a notion challenged by Coppieters et al. [4], Kraus et al. [5] and Gil et al. [6], both considered the friction coefficient to be variable with pressure during testing. Siebel és Christiansen et al. [7] proposed a flow curve equation compensation for geometric considerations in compaction testing. During the Watts–Ford-test Graf et al. [8], Chermette et al. [9] and Banabic et al. [10] also made recommendations regarding the relationship between various geometric dimensions of the test specimen.

Geometric correction is not only important for proper approximation of flow curves but also for describing anisotropic plastic behaviour, where the test specimen deforms non-uniform-

ly in different directions. Anisotropic behaviour is known from fracture tests, where the ratio of cross-directional and thickness-directional deformations of the sheet specimen is referred to as the anisotropy factor. However, in mechanically equivalent biaxial tensile stress states achieved with uniaxial compression, the sheet may behave differently. In the literature, the proportion of in-plane deformations measurable during experiments conducted under such stress states is termed biaxial, or two-directional, anisotropy factor [1]. It is necessary, however, to examine the dependence of this measure on factors known to influence the formation of flow curves during compression. These factors include friction and the length-to-diameter ratio. In this article, we focus on the effect of the latter factor.

2. Preparation and execution of the experiments

The tests were conducted on sheet material labelled DC04, which, due to its ferritic microstructure, endows it with good formability properties, making it widely used in various industries.

2.1. Presentation of test specimen

The test specimens were fabricated from sheet metal. Cutting was performed using the Trumpf TruLaser Cell 7020 system, a 4 kW diode laser-based equipment. The cutting accuracy of the device is ± 0.02 mm. Nitrogen gas was used during cutting.

Considering the cross-section of the selected test specimen to be circular, its nominal diameter is 10 mm, and its nominal thickness is 1 mm. The precise dimensions of diameter and thickness were determined from the average of fifty test specimen geometries. The rolling direction of the sheet was always marked.

2.2. Presentation of testing equipment

The experiments were conducted using the INSTRON 4482 electromechanical universal testing machine, capable of applying tensile, bending, shear, and compression loads, and determining strength and plasticity characteristics. The INSTRON 4482 testing machine is shown in [Figure 1](#).

We equipped the machine with cylindrical pressure plates, with a diameter of 40 mm and a thickness of 20 mm. The pressure plates were made of highly alloyed tool steel designated as K110, which had an average hardness of 57 HRC after heat treatment. The pressure surfaces were



Fig. 1. Instron4482 electromechanical universal testing machine.



Fig. 2. The polished pressure plates.

polished, as shown in [Figure 2](#). This was necessary to reduce the friction between the workpiece and the tool.

2.3. Positioning and lubrication

During the experiment, it is crucial to ensure the uniaxial alignment of the specimens. Manual positioning is not sufficient, so we created a positioning unit using additive manufacturing on the Craftbot flow index xl device. The material used is BASF's PLA, and it consists of two halves. When closed, the surfaces of the test specimens and the inner walls of the positioning device create point-like contact, reducing the degree of uniaxial error. The unit and the disk assembly it arranges can be seen in [Figure 3](#) displaying the unit's length-to-diameter (l/d) ratio.

The surfaces of the test specimens in contact with the pressure plates were treated with Luba 21 high-pressure lubricant. However, no lubrication was applied to the surfaces of the test specimens in contact with each other, aiding in promoting bulk material behavior.

2.4. Execution of compression tests

The experiments were conducted for three different cases. In the first case, a single disk (length-to-diameter ratio: 0,1) was used, in the second case, five disks (length-to-diameter ratio: 0,5), and in the third case, ten disks (length-to-diameter ratio: 1,0) were stacked and subjected to compaction tests at a constant strain rate, with a threefold frequency of measurements. A test specimen between the pressure plates can be seen in **Figure 4**.

The displacement of the crosshead occurred at a rapid traverse speed of 3 mm/min, while the preload did not reach 250 N. This value corresponds to compressive stresses of 3–10 MPa, which is less than 5% of the yield strength but sufficient to stabilize the assembly before the main loading begins. Subsequently, the crosshead proceeded depending on the height of the assemblies, ensuring the following relationship is fulfilled.

$$v = h/10, \quad (1)$$

where v is the displacement speed of the crosshead, and h is the initial height of the currently compacted assembly.

In **Figure 5** the assemblies are visible after compaction. The compression of each assembly continued until we approximately reached half of the initial height.

2.5. Scanning and measurement of test specimens

Subsequently, the scanned images of the compacted test specimens were obtained using the Vinyl Open Air device. The equipment employs a single camera with a resolution of 1.3 megapixels and capable of achieving an accuracy of 6 μm . The test specimens were fixed to the machine's magnetic table. The point cloud generated during scanning is depicted in **Figure 6**. The point clouds contain the coordinate points of the entire assemblies after compaction.

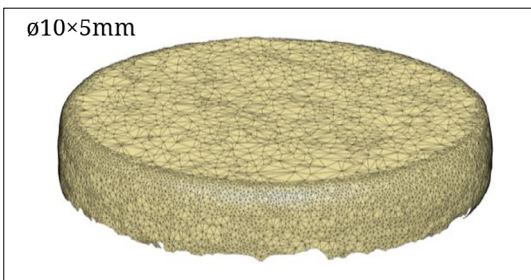


Fig. 6. The scanned specimen.

We reduced the number of elements in the scanned point cloud, helping to speed up modelling. The model based on the simplified point cloud is shown in **Figure 7**.

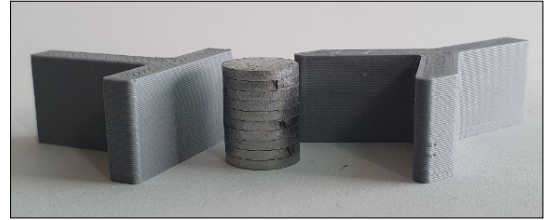


Fig. 3. Positioning unit and the stack made by it.

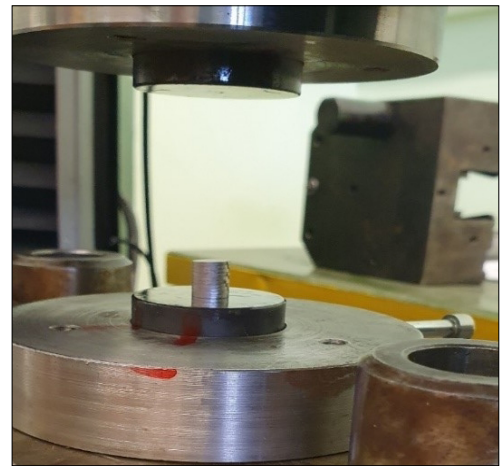


Fig. 4. Execution of the compression tests.



Fig. 5. The stacks after compression test.

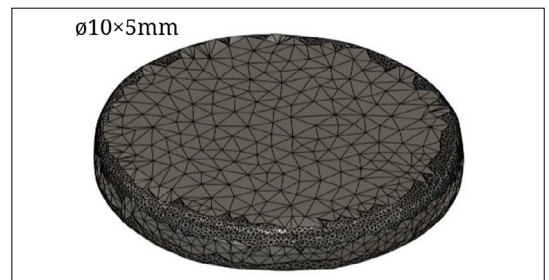


Fig. 7. The model based on the simplified point cloud.

3. Results

The necessity of scanning plays a role in measuring deformations occurring during compression tests. While we can directly calculate the thickness-directional deformation (ϵ_v) of the test specimens during testing from the values of the crosshead displacements (taking into account the stiffness of the machine), the in-plane deformations remain hidden between the pressure plates. (For the calculation of thickness-directional deformations, we used the statistical sheet thickness as the initial size.)

By measuring the in-plane deformations, we can infer the anisotropic behavior of the test specimens. An example of this can be seen in **Figure 8**, where the parallel (ϵ_ρ) and perpendicular ($\epsilon_{\rho 0}$) logarithmic deformations to the rolling direction are clearly different. A difference of nearly one millimeter is observed between certain dimensions of the test specimen at a 0,5 l/d ratio.

The calculation of effective, true plastic deformations (ϵ_f) is possible based on the knowledge of the flow condition (assumption), for which in this study, we applied the Hill'48 theory [11]. For this purpose, only the in-plane principal deformations and the average normal anisotropy factor (R value) obtained from tensile tests need to be known, which, based on our previous measurements, can be assumed to be 1.706 for the DC04 material. In **Table 1**, β expresses the ratio of in-plane principal deformations, which is also equal to the value of the biaxial elongation anisotropy factor (r_b):

$$r_b \equiv \beta = \frac{\epsilon_{90}}{\epsilon_0} \tag{2}$$

The values of the anisotropy factors for tensile testing and biaxial elongation can be illustrated by **Figures 9** and **10**.

During tensile tests, the normal anisotropy factor varies slightly as deformation progresses, as shown in **Figure 9**. Approximating with a linear function, we provided the average of three measurements in the text.

Based on **Figure 10**, the value of anisotropy associated with biaxial elongation can also be considered variable depending on the geometric ratio or the effective deformation.

4. Conclusions

A convenient method for capturing flow curves in large deformation ranges is compaction testing. However, its execution requires geometric and frictional corrections.

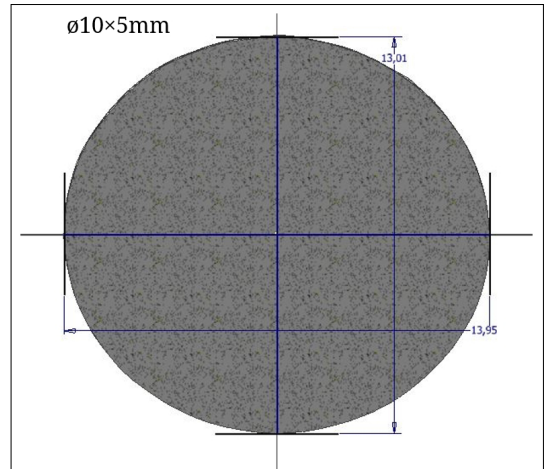


Fig. 8. The difference in diameter between the rolling direction and the perpendicular direction.

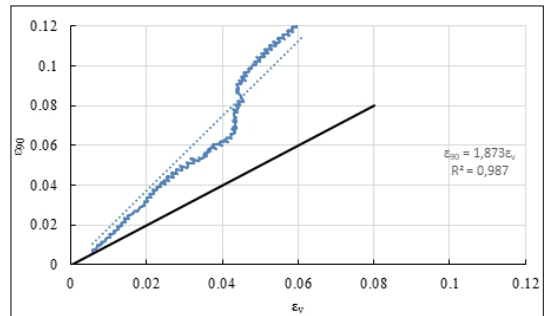


Fig. 9. Anisotropy (R) Value Determined from Tensile Testing.

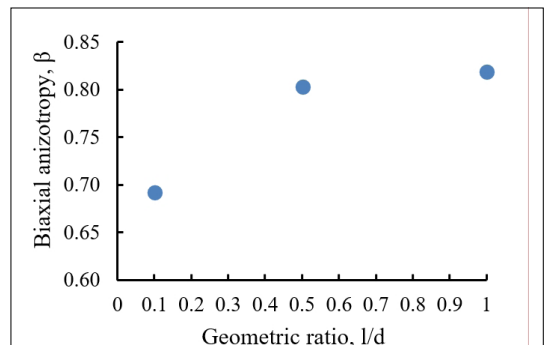


Fig. 10. The change in biaxial anisotropy (R) value as a function of the l/d ratio.

Table 1. The measured and calculated deformations

l/d	ϵ_v	ϵ_0	ϵ_{90}	ϵ_f	β
0.1	-0.355	0.241	0.167	0.476	0.69
0.5	-0.633	0.356	0.286	0.748	0.80
1.0	-0.675	0.370	0.303	0.784	0.82

In our study, we examined whether it is necessary to consider the geometric ratio when determining the biaxial anisotropy factor or if it only distorts the shape of the flow curves. We conducted our investigations on test specimens with l/d ratios of 0.1, 0.5, and 1.0. Deformations were derived from changes in mid-diameter using digital image correlation.

Our results indicate that the measured value of the biaxial anisotropy factor is slightly distorted in the examined geometric ratio and deformation range when the length-to-diameter ratio is small (in our case, 0.1). However, significant differences are not observed for length-to-diameter ratios of 0.5 and above.

References

- [1] Barlat F., Brem J. C., Yoon J. W., Chung K., Dick R. E., Lege D. J., Pourboghrat F., Choi S.-H., Chu E.: *Plane stress yield function for aluminum alloy sheets – Part 1: theory*. Int. J. Plast., (2003) 1297–1319.
[https://doi.org/10.1016/S0749-6419\(02\)00019-0](https://doi.org/10.1016/S0749-6419(02)00019-0)
- [2] Coppieters S., Traphöner H., Stiebert F., Balan T., Kuwabara T., Tekkaya A. E.: *Large strain flow curve identification for sheet metal*. J. Mat. Pro. Tec., 308. (2022) 117725.
<https://doi.org/10.1016/j.jmatprotec.2022.117725>
- [3] Merklein M., Kuppert A.: *A method for the layer compression test considering the anisotropic material behavior*. Int. J. Mater. Form., 2. (2009) 483–486.
<https://doi.org/10.1007/s12289-009-0592-8>
- [4] Coppieters S., Lava P., Sol H., Van Bael A., Van Houtte P., Debruyne D.: *Determination of the flow stress and contact friction of sheet metal in a multi-layered upsetting test*. J. Mat. Pro. Tec., 210. (2010) 1290–1296.
<https://doi.org/10.1016/j.jmatprotec.2010.03.017>
- [5] Kraus M., Lenzen M., Merklein M.: *Contact pressure-dependent friction characterization by using a single sheet metal compression test*. Wear, 476. (2021) 203679.
<https://doi.org/10.1016/j.wear.2021.203679>
- [6] Gil I., Mendiguren J., Galdos L., Magurra E., Ar-gandona E. S. de: *Influence of the pressure dependent coefficient of friction on deep drawing spring-back prediction*. Tribology International, 103. (2016) 266–273.
<https://doi.org/10.1016/j.triboint.2016.07.004>
- [7] Christiansen P., Martins P. A. F., Bay N.: *Friction Compensation in the Upsetting of Cylindrical Test Specimens*. Experimental Mechanics, 56. (2016) 1271–1279.
<https://doi.org/10.1007/s11340-016-0164-z>
- [8] Graf M., Fritsch S., Awiszus B.: *Determination of Forming Behaviour of EN AW-6060 by Different Testing Methods under Cold Bulking Forming Conditions*. Procedia Manufacturing, 47 (2020) 1512–1519.
<https://doi.org/10.1016/j.promfg.2020.04.339>
- [9] Chermette C., Unruh K., Peshekhodov I., Chottin J., Balan T.: *A new analytical method for determination of the flow curve for high-strength sheet steels using the plane strain compression test*. Int. J. Mater. Form., 13. (2020) 269–292.
<https://doi.org/10.1007/s12289-019-01485-4>
- [10] Banabic D., Bunge H.-J., Pöhlandt K., Tekkaya A. E.: *Formability of Metallic Materials*. Springer-Verlag, 2000.
<https://doi.org/10.1007/978-3-662-04013-3>
- [11] Hill R.: *A theory of the yielding and plastic flow of anisotropic metals*. Royal Society, 193. (1948) 1033.
<https://doi.org/10.1098/rspa.1948.0045>



Application of 3PHV60 Type Epoxy Resin for the Repair of Timber Structures

Péter MÁRTON

Technical University of Cluj-Napoca, Faculty of Civil Engineering, Doctoral School, Cluj-Napoca, Romania, marton.peter17@gmail.com

Abstract

This article deals with the issue of repairing wooden structures with 3PHV60 type resin. The first step of the research was to understand the material properties of 3PHV60 resin. The information provided by the resin manufacturer and the tests based on fracture tests have greatly contributed to the proper study of the behaviour of this material. The use of resin for the repair of timber structures is discussed in relation to the type of internal forces.

Keywords: *structural timber, epoxy resin, timber repair, reconstruction, restoration.*

1. Introduction

Many times during the renovation of an existing building, the question of consolidation of the wooden bearing structures arises. To this end, a number of solutions are used in practice, in terms of the use of materials or the degree of intervention.

The central question of the research is whether the resin type 3PHV60 can be suitable for the local repair of wooden structures.

In this paper, I will present experiments on 3PHV60 resins. I will then focus on the consolidation of wood with resins, grouped according to the type of stresses. The tests are based on fracture tests.

2. General description of 3P type epoxy resin

3P resins are two-component systems, which are copolymers of polyisocyanate/waterglass. 3P resins are named after the initial letters of the Anglo-German words for their components: polysilicic acid, polyisocyanates, phosphoric acid esters [1].

The „A” component of hard 3P resins is always Na-waterglass and the „B” component is MDI (methylene diphenyl isothiocyanate and its derivatives) [1].

The production of 3P resin starts with a simple but careful mixing of components A and B. The

two components are homogenised in a volume ratio of 1:2 (Figure 1).

The resin is considered homogeneous when the total volume has become a uniform latte colour.

3. Material properties of 3PHV60 type epoxy resin

3PHV60 is a type of hard resin, a subtype of type 3P resins. Break tests were carried out to determine the material properties. Part of the tests were carried out at Polinvent KFT in Gyál, the other part at the Adolf Czakó Laboratory of Strength of Materials of the Budapest University of Tech-



Fig.1. The „A” and „B” components of 3P resin.

nology and Economics. All resin specimens were tested at least on the 7th day after their manufacture.

3.1. Determination of tensile strength of resin type 3PHV60

I used a mould to produce the specimens used to determine the tensile strength of the resin. The liquid resin was poured into the mould as shown in **Figure 2** and after 7 days it was broken off using a Zwick Roell Z150 (**Figure 3.**) at the BME Laboratory of Strength of Materials.

3PHV60 is a type of hard resin, a subtype of type 3P resins. Break tests were carried out to determine the material properties. Part of the tests were carried out at Polinvent KFT in Gyál, the other part at the Adolf Czákó Laboratory of Strength of Materials of the Budapest University of Technology and Economics. All resin specimens were tested at least on the 7th day after their manufacture.

Table 1 summarises the force at fracture (F_{max}), from which, knowing the cross-section (A), the normal stress (σ_f) at the moment of fracture can be determined.

The average normal stress at fracture is 19.46 N/mm^2 , with a standard deviation of 1.92 N/mm^2 .

Table 1. Tensile test results of resin specimens at fracture

#	F_{max} (N)	A (mm^2)	σ_t (N/mm^2)
1	719.58	42.36	16.99
2	826.58	41.12	20.10
3	846.67	46.59	18.17
4	861.33	48.29	17.83
5	1063.34	49.08	21.67
6	1102.94	50.14	22.00

3.2. Determination of shear strength of resin type 3PHV60

To determine the shear load capacity of the 3PHV60 resin, 5 specimens of $20 \times 20 \times 120 \text{ mm}$ geometry were prepared. The breaking test was carried out on day 7 after casting.

Table 2 summarises the force at fracture (F_{max}), from which the maximum shear force (V_{max}), can be calculated and, knowing the sheared area (A), the shear stress (τ) can be calculated.



Fig. 2. Test specimens used to determine the tensile strength of the resin.



Fig. 3. Measurement of tensile strength of resin.

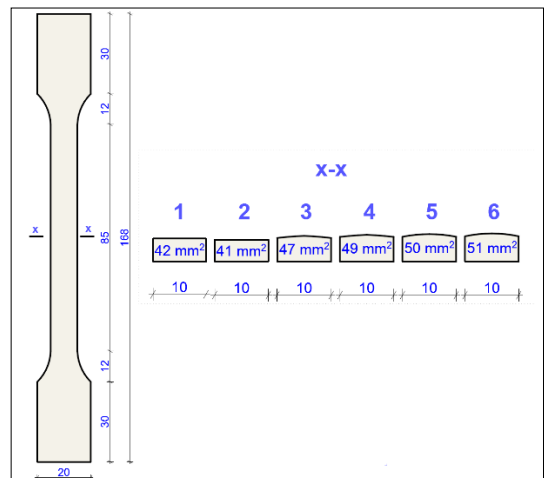


Fig. 4. Resin specimens tested in tension.

Table 2. Shear test results of resin specimens at fracture

#	F_{max} (N)	V_{max} (N)	A (mm ²)	τ (N/mm ²)
1	12 884	6442	400	16.11
2	12 114	6057	400	15.14
3	11 935	5967	400	14.92
4	10 882	5441	400	13.60
5	12 272	6136	400	15.34

The average shear stress at fracture is 15.02 N/mm² at a deviation of 0.81 N/mm².

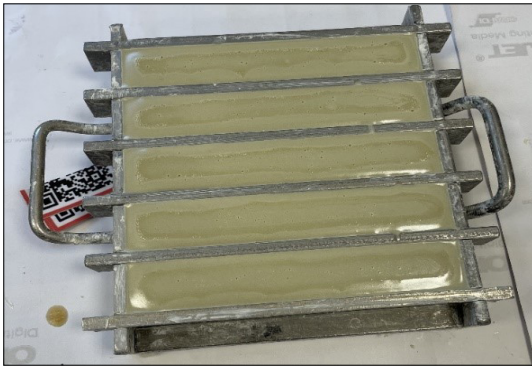


Fig. 5. Resin specimens to be tested in shear at the beginning of the setting phase.

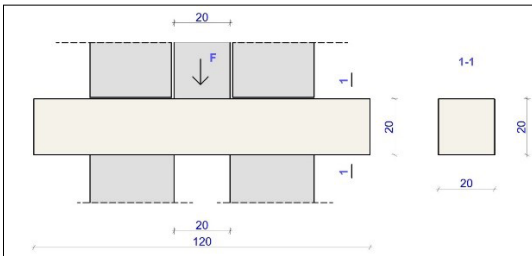


Fig. 6. Resin test specimen shear test.

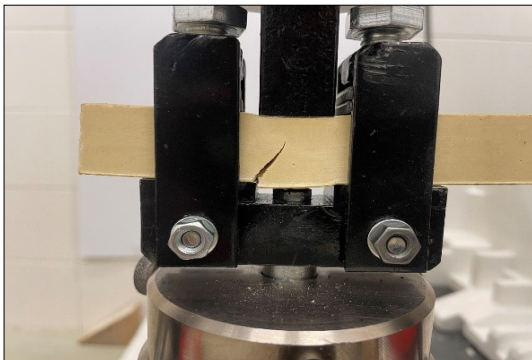


Fig. 7. Typical fracture pattern of resin specimens tested in shear.

3.3. Determination of the moment capacity of resin type 3PHV60

For the determination of the moment capacity of the 3PHV60 resin, the standard MSZ EN 13982-2:2003 was used, which provides guidance on the geometry of the specimens and the conduct of the fracture tests.

The breaking tests were carried out with the Instron breaking machine of the resin manufacturer Polinvent Ltd.

5 specimens with a geometry of 20×20×120 mm were made and loaded with a concentrated force at half the span.

Table 3 summarises the force at fracture (F_{max}), from which the maximum bending moment can be calculated (M_{max}), and, knowing the section modulus (W) the bending stress (σ_m) can be calculated.



Fig. 8. Resin specimen tested for bending.

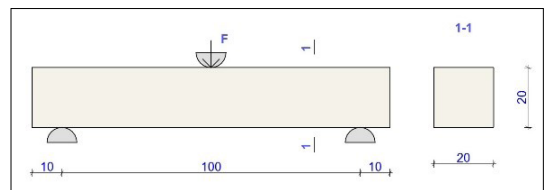


Fig. 9. The sketch of the bending strength test of resin.

Table 3. Fracture results of resin specimens tested for bending

#	F _{max} (N)	M _{max} (Nmm)	W (mm ³)	σ _m (N/mm ²)
1	2228	55 710	1.333	41.78
2	2433	60 825	1.333	45.63
3	2496	62 400	1.333	46.82
4	2420	60 500	1.333	45.39
5	2467	61 675	1.333	46.26

The resin has an average bending strength of 45.63 N/mm² at a standard deviation of 1.76 N/mm².

From the force-displacement diagram, we can observe that a brittle fracture has occurred here too.

3.4. Determination of the local compressive strength of resin type 3PHV60

To determine the local compressive strength of the resin, I tested the specimens used in the bending strength experiments. Again, the behaviour of 5 specimens was measured, loaded on a 20×20 mm surface.

In Table 4 I have summarized the compression at maximum force (dH) and the normal stress value from local compression (σ_{pecset}).

Table 4. Results of local compression tests on resin specimens.

#	F _{max} (kN)	A (mm)	dH (mm)	σ _{pecset} (N/mm ²)
1	2228	400	1.333	73
2	2433	400	1.333	75
3	2496	400	1.333	76
4	2420	400	1.333	74
5	2467	400	1.333	76

The average value of the stresses from local compression is 75 N/mm², with a standard deviation of 1.16 N/mm².

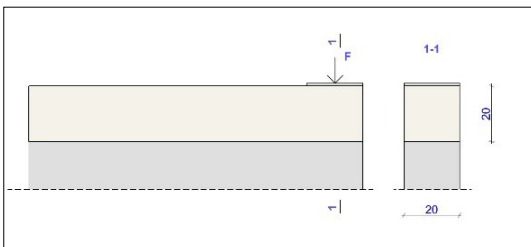


Fig. 10. Outline of the local compression strength test of resin.

4. Use of 3PHV60 epoxy resin on soft-wood structural elements

To determine the applicability of the resin on wood, I carried out the following experiments:

- Adhesion tests of wood-epoxy resin (sectional, parallel to grain and perpendicular to grain);
- Shear load tests;
- Bending load capacity tests.

At the time of writing, a compression load test is still in preparation, and the resin is in the process of setting.

For the experiments I used specimens of common spruce (picea abies) below 12% relative humidity.

4.1. Adhesion test of 3PHV60 type resin and wood on the sectional side

The test specimens illustrated in Figure 11 were used to test the adhesion of the resin and wood on the sectional side of the wood. The 2 20×40 mm sectional faces of the wood were coated with resin and the two specimens were then joined together to give a 1600 mm² adhesion area. After the 7 day resin curing period, the fracture tests were carried out.

In terms of resin consistency, this study was split into two parts. In the first series, a very liquid resin, at the very beginning of the setting phase, was applied to the sectional side of the wood. In the second series, a more viscous resin, more advanced in the setting phase, was applied to the sectional faces of the wood specimens.

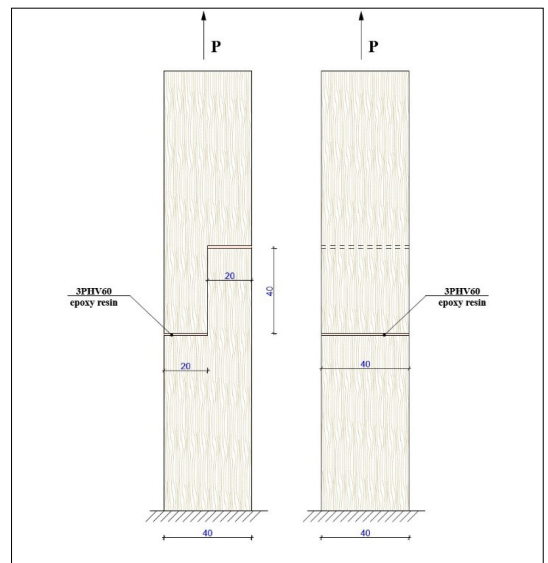


Fig. 11. Adhesion test of the resin and wood on the sectional side of the wood.



Fig. 12. Adhesion testing of resin applied on the sectional side of the wood.

Table 5. Result of the adhesion testing on the sectional side, Series 1.

#	F_{max} (N)	A (mm)	Sectional adhesion (N/mm ²)	Average adhesion (N/mm ²)
1	2756	1600	1.72	2.70
2	4286	1600	2.67	
3	5263	1600	3.28	
4	5056	1600	3.16	
5	3850	1600	2.40	
6	4909	1600	3.06	
7	3367	1600	2.10	
8	5172	1600	3.23	

Table 6. Result of the adhesion testing on the sectional side, Series 2.

#	F_{max} (N)	A (mm)	Sectional adhesion (N/mm ²)	Average adhesion (N/mm ²)
9	6977	1600	4.36	5.04
10	6102	1600	3.81	
11	7988	1600	4.99	
13	10248	1600	6.40	
14	9070	1600	5.66	

The average adhesion on the sectional side of the wood obtained in the second series is 86% higher than the average value obtained in the first series.

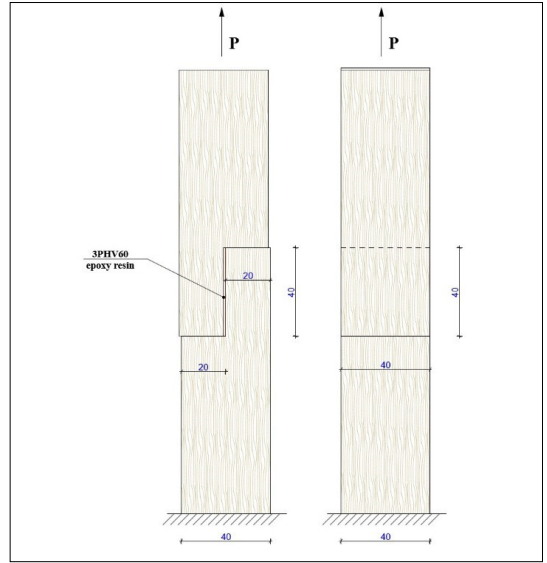


Fig. 13. Test specimens for fibre adhesion testing of resinous wood.

4.2. Adhesion test of resin type 3PHV60 and wood parallel to grain

For the fibre direction adhesion test of resin and wood, similar specimens were used as in the previous test, except that this time the sides of the wood specimens parallel to the fibre direction were coated with resin (Figure 13). After waiting for 7 days of curing time, the specimens were loaded with the breaking machine until the resin-timber bond was destroyed.

In the case of the fibre adhesion test, 8 specimens were taken and the fracture results are summarised in Table 7.

The results of the second series of adhesion test on the sectional side of the wood are similar to the results of the fibre adhesion tests.

Table 7. Resin-timber fibre directional adhesion

#	F_{max} (N)	A (mm)	Fibre directional adhesion (N/mm ²)	Average adhesion (N/mm ²)
1	7865	1600	4.91	4.80
2	7049	1600	4.40	
3	7753	1600	4.84	
4	4631	1600	2.89	
5	7529	1600	4.70	
6	10692	1600	6.68	
7	7488	1600	4.68	
8	8494	1600	5.30	

4.3. Adhesion tests of resin type 3PHV60 and wood perpendicular to grain

In this experiment, 8 specimens were also made with the same adhesion surface (A), as in the previous two adhesion tests. The bonded specimens have an adhesion area of 40×40 mm².

Table 8. Epoxy-resin wood adhesion perpendicular to grain

#	F _{max} (N)	A (mm)	Adhesion perpendicular to grain (N/mm ²)	Average adhesion (N/mm ²)
1	5379	1600	3.36	3.20
2	4705	1600	2.94	
3	5054	1600	3.15	
4	6941	1600	4.33	
5	4449	1600	2.78	
6	4912	1600	3.07	
7	4437	1600	2.77	
8	5032	1600	3.14	

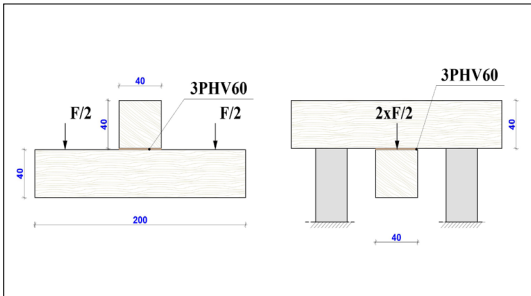


Fig. 14. Adhesion test of the resin 3PHV60 and wood perpendicular to grain/



Fig. 15. Measuring the adhesion of resin and wood perpendicular to grain.

In the case of the perpendicular adhesion test, the wooden test specimens are used for tension perpendicular to grain. In this test, failure typically occurs in the wood and not at the interface between the resin and the wood. This is not surprising, as the strength properties of wood are the lowest in the perpendicular tensile load.

4.4. Testing of shear loads

To test the shear load capacity of resin reinforced wood, 3 series of measurements were taken and compared after the measurements.

4.4.1. Shear load test of a full cross-section timber specimen

In this series, my goal was to obtain data on the average shear load of the tested wood. Then, in the following series, using this wood, we will model weakening on the test specimens, followed by improvement of weakening in practice.

8 wooden specimens of 40×40×120 mm solid cross-section were produced, the test is illustrated in [Figure 17](#).

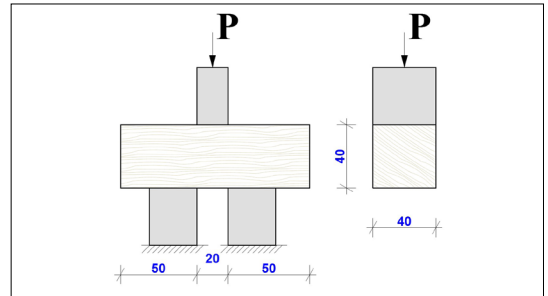


Fig. 16. Outline of the full cross-section sheared wood test specimen experiment.

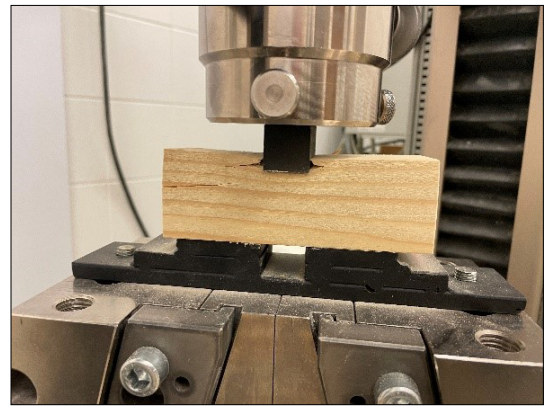


Fig. 17. The full cross-section sheared wood specimen.

Table 9 summarises the measured shear load values. The average shear stress at the moment of failure is 5.03 N/mm², with a standard deviation of 0,45N/mm².

The value of the maximum shear force (V_{max}) is equal to half the force P_{max} applied at the moment of fracture.

Table 9. Shear strength of full section timber specimens

#	V_{max} (N)	A (mm)	Shear strength (N/mm ²)	Average shear strength (N/mm ²)
1	8693	1600	5.43	5.03
2	7664	1600	4.79	
3	8148	1600	5.09	
4	9187	1600	5.74	
5	7518	1600	4.70	
6	6817	1600	4.26	
7	7743	1600	4.84	
8	8623	1600	5.39	

The average of breaking forces measured here are 16 098 N.

4.4.2. Investigation of the shear strength of weakened cross-sectional timber specimens

For the measurement, seven specimens of 40×40×120 mm, as used in the previous subsection, were prepared, on which a regular geometry cross-section reduction was applied in the shear-loaded section. In the loaded section, I removed a 20×20×40 mm section of the wood.

In this case, the shear-resistant wood cross-section area is reduced to 800 mm².

Table 10. Shear strength of weakened cross-sectional timber specimens

#	P_{max} (N)	V_{max} (N)	A (mm)	Shear strength (N/mm ²)	Average shear strength (N/mm ²)
1	13 378	6689	800	8,36	8,53
2	15 329	7664	800	9,58	
3	16 570	8285	800	10,35	
4	17 110	8555	800	10,69	
5	11 542	5771	800	7,21	
6	11 747	5873	800	7,34	
7	9 861	4930	800	6,16	

The average breaking forces measured here are 13648 N.

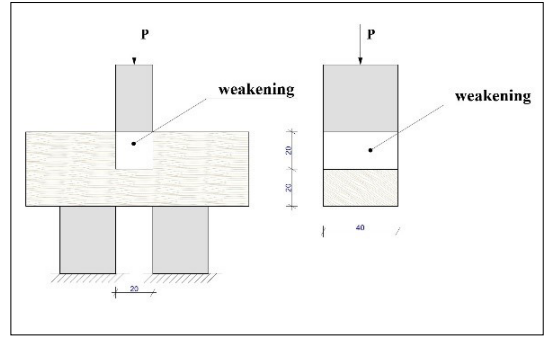


Fig. 18. Shear load test with weakening.



Fig. 19. Shear load test with weakening.

4.4.3. Shear strength testing of resin supplemented weakened wood specimens

Regular „weakened” specimens formed on the test specimens described in section 4.4.2 were filled with 3PHV60 resin and then these specimens were also broken while waiting for the resin to set.

Table 11. Shear strength of weakened cross-section timber specimens filled with epoxy resin

#	P_{max} (N)	V_{max} (N)	Average shear force (N)	Average breaking force (N)
1	20 531	10 265	9 313	18 626
2	18 096	9 048		
3	21 734	10 867		
4	17 129	8 564		
5	15 327	7 663		
6	18 014	9 007		
7	18 204	9 102		
8	19 983	9 991		

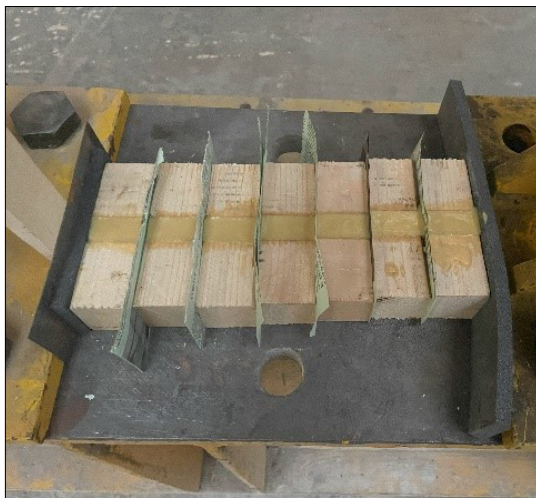


Fig. 20. Shear test specimens supplemented with resins.



Fig. 21. Shear test specimens supplemented with resins.

The average value of the breaking forces for the resin-filled weakened specimens was 18626 N, while for the full cross-section intact wood specimens it was 16098 N.

4.5. Bending load capacity tests

For the bending load tests, I used the standard [4] MSZ EN 408:2010+A1:2012, which specifies the geometrical and loading parameters required for the bending load tests. Several series were performed for this test as well as for the determination of shear load capacities. By comparing the series I try to draw conclusions about the effectiveness of the methods. In these tests I compare the forces at the moment of fracture, not the bending stresses.

4.5.1. Bending load capacity of the specimens weakened in the bottom side

I measured 5 specimens of 40×40×800 mm geometry with a span of 720 mm. I loaded the specimens at the thirds of the span. At half of the span, a regular cross-section weakening was carried out by cutting a 40×20×20 mm body from the bottom side of the specimens.

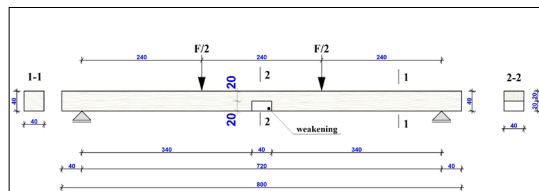


Fig. 22. Bend capacity test of resin-filled specimens weakened in the bottom side.

Table 12. Breaking forces for weakened test specimens in the bottom side

#	P_{\max} (N)	Average of breaking forces (N)
1	1395	801.30
2	411	
3	658	
4	549	
5	991	

4.5.2. Bending load capacity of resin-filled specimens weakened in the bottom side

The specimens used in section 4.5.1 were taken as a basis. The weakened section was filled with resin and the forces at the moment of fracture were measured after the 7-day setting time.

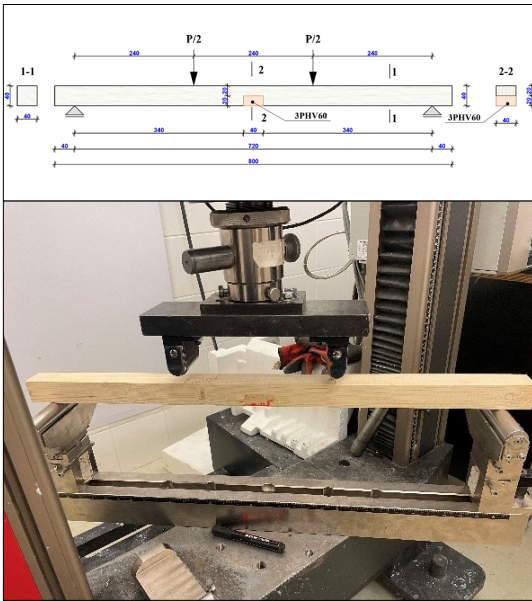


Fig. 23. Bend capacity test of resin-filled specimens weakened in the bottom side.

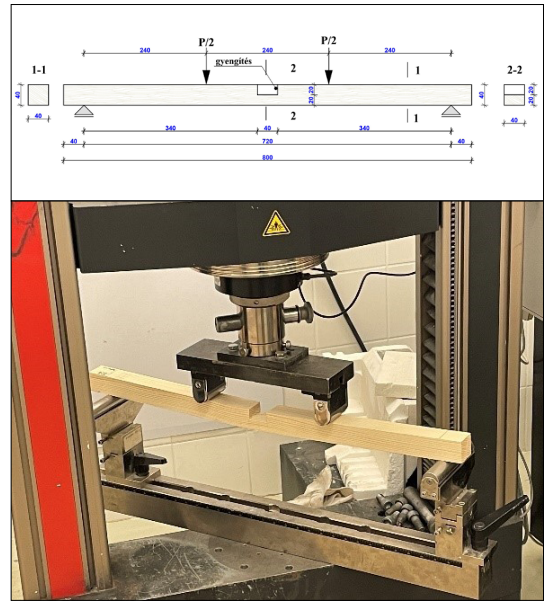


Fig. 24. Test of the bending capacity of timber specimens weakened in the upper side.

Table 13. Summary of lower-belt weakened, resin-reinforced test specimens

#	P_{max} (N)	Average of breaking loads (N)
1	1730	1243.17
2	1064	
3	1650	
4	1285	
5	1032	
6	696	

4.5.3. Bending load capacity of specimens weakened in the upper side

As in section 4.5.1, 5 specimens were made, with the difference that this time the weakening was applied in the upper belt.

Table 14. Summary of upper-side weakened test specimen breaking loads

#	P_{max} (N)	Average of breaking loads (N)
1	942	1304
2	1024	
3	1581	
4	1578	
5	1386	

4.5.4. Bending load capacity of resin-filled specimens weakened in the upper side

7 test specimens similar to 4.5.3 were prepared, with cross-sectional weakening filled with resin. In my study *A Régi fa tartószerkezeti elemek állapotfelmérése roncsolásmentes, illetve töréskén alapuló vizsgálatokkal* [5], presented at the Conference on Civil Engineering and Architecture in 2019, the average value of the breaking forces of the unweakened specimens (32 specimens) was 4566N.



Fig. 25. Filling the weakened timber parts with epoxy resin.

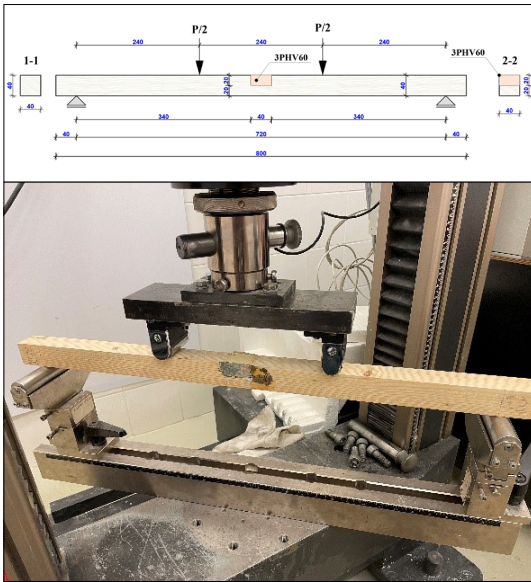


Fig. 26. Investigation of the bending capacity of resin reinforced timber specimens weakened in the upper side.

Table 15. Summary of upper-side weakened resin-filled timber test specimens

#	P_{\max} (N)	Törési erők átlaga (N)
1	4009	4387
2	4092	
3	4860	
4	4446	
5	3413	
6	4194	
7	5693	

5. Conclusions

Through the measurements presented in this study, I gained insight into the potential of using 3PHV60 resin in the restoration of damaged timber structures.

The primary objective of the adhesion test measurements was to investigate the use of resin to repair tensioned timber structural members and joints.

For the reinforcement of weakened or, in practice, mechanically damaged wood elements subject to shearing, the use of the 3PHV60 resin I have tested may be a good alternative. The addition of resin to the reduced timber cross-section resulted in higher shear load capacities than the full cross-section timber specimens.

For timber structural members subjected to bending, a very important issue is whether the damage is on the tension or compression side of the timber. If the damage is on the compressive side, the original bending strength of the wood can be recovered by filling with resin. If the damage is on the tensile side, filling the mechanically damaged area with resin may improve the bending strength, but other applications (e.g. glued steel or composite sheet) to be tested later may be required to restore the original strength.

Acknowledgement

I am grateful to Dr. Miklós Armuth, Professor (Budapest University of Technology and Economics), Ottó Sebestyén, Technician (Budapest University of Technology and Economics), Dániel Karádi, PhD student in architecture (Budapest University of Technology and Economics), Miklós Baróthy, Chemical Engineer (Polinvent KFT) and Prof. Dr. Gábor Köllő (Technical University of Cluj-Napoca), who helped and supported me in the appropriate phases of my study.

References

- [1] Nagy G. F.: *A Polinvent Kft. direkt és indirekt polikarbamid (PU) rendszerei*. Gyál, 2012.
- [2] MSZ EN 13892-2:2003 Esztrichek és padozati anyagok vizsgálati módszerei, 2. rész: A hajlító-húzó és a nyomószilárdság meghatározása
- [3] MSZ EN 13892-1:2003 Esztrichek és padozati anyagok vizsgálati módszerei, 1. rész: Mintavétel, vizsgálati próbatestek készítése és tárolása
- [4] MSZ EN 408:2010+A1:2012 Faszerkezetek. Szerkezeti fa és rétegelt-ragasztott fa. Egyes fizikai és mechanikai tulajdonságok meghatározása
- [5] Márton P.: *Régi fa tartószerkezeti elemek állapotfelmérése roncsolásmentes, illetve töréseken alapuló vizsgálatokkal*. XXIII. Nemzetközi Építéstudományi Konferencia, Erdélyi Magyar Műszaki Társaság, Csíksomlyó, 100–102.



Examination of a Hot-Work Tool Steel Treated with Different Nitriding Processes after Cyclic Heating

Klaudia OLÁH,¹ Krisztián KORSÓS,² Dorina KOVÁCS³

¹ *Budapest University of Technology and Economics, Faculty of Mechanical Engineering, Department of Materials Science and Technology, Budapest, Hungary, olah.klaudia@edu.bme.hu*

² *Budapest University of Technology and Economics, Faculty of Mechanical Engineering, Department of Materials Science and Technology, Budapest, Hungary, krisztian.korsos@edu.bme.hu*

³ *Budapest University of Technology and Economics, Faculty of Mechanical Engineering, Department of Materials Science and Technology, Budapest, Hungary, kovacs.dorina@gpk.bme.hu*

Abstract

This research examines the effect of salt bath, and nitriding processes on hot forming tool steel. The chosen steel is BÖHLER W350 ISOBLOCK hot forming tool steel, which is widely used in the industry for pressure casting. After surface treatment, some samples were exposed to cyclic heat and corrosion effects in a molten aluminium medium, thus simulating the conditions experienced during pressure casting. Microhardness measurements were performed on the samples treated with different procedures. The results were compared using a scanning electron microscope and energy-dispersive X-ray spectrometry.

Keywords: *plasma nitriding, salt bath nitriding, hot work tool steel.*

1. Introduction

Today, aluminium castings account for a significant proportion of automotive components. Aluminium is a light metal that enables the production of light machine parts without deterioration of their strength characteristics.

In the production of these parts, the casting tool plays a prominent role: even when used at high temperatures, it must show high resistance to both mechanical and corrosion effects. The industry uses hot-forming tool steel as the raw material for casting tools, which retains its heat resistance even at the melting point of aluminium. In order to preserve the quality of the tool in the long term, its surface treatment is essential.

Nitriding is a thermochemical surface treatment during which nitrogen is diffused into the surface of the workpiece in order to create a hard, wear-resistant layer containing nitrides [1, 2]. Many versions of nitriding are used in different industries in accordance with the requirements of the given area of use.

Previous research has reported an improvement in the thermal fatigue life of 1.2343 and 1.2344

steels after various nitriding treatments [3, 4]. Yucel Birol [5] investigated the effect of plasma nitriding against thermal fatigue for 1.2365 steel. During the thermal fatigue test between 450 °C and 750 °C lasting 500 cycles, the original surface hardness of the surface treated steel 1084 HV0.02 decreased to 250 HV0.02. The authors attributed the phenomenon to the thermal damage of the surface compound layer, the decrease in nitrogen content, and the microstructural transformation of the substrate.

In other research, Guang Chen et al [6] performed a similar experiment on steel number 1.2344 surface treated by salt bath nitriding at different temperatures (430, 450 and 470 °C) and treatment time (4, 6 and 8 hours). The specimens were held in molten aluminium at 750 °C for 30 minutes. As a result of their research, it can be concluded that the hardness values of the samples decreased from 1050-1317 HV0.1 to 855-891 HV0.1.

However, no literature data compares the two nitriding processes based on the results of thermal fatigue experiments performed under the same conditions. During our research, the cyclic

thermal fatigue test was performed on specimens treated with plasma nitriding and salt bath nitriding, and then the treatment procedures in terms of the decrease in hardness values and the change in nitrogen concentration were compared.

2. Research methodology

2.1. The examined steel and its treatments

The material examined during the research was BÖHLER W350 ISOBLOCK hot forming tool steel, whose chemical composition is shown in [Table 1](#).

The raw material was obtained as a steel bar with a cross section of 20×20 mm, then cut into 5 mm thick test pieces with a water-cooled abrasive cutting disc cutting machine. This type of steel is precipitation hardenable, so to reach its desired hardness, three annealing steps must be performed in its heat treatment cycle. The third annealing temperature coincides with the nitriding temperature, so the two processes were performed in one step. The preliminary heat treatment of the test specimens is shown in [Figure 1](#).

The salt bath treatment was carried out in a carbonitriding medium with a low cyanide content at 580 °C for 2.5 hours. Plasma nitriding was carried out at 520 °C in a 1:3 nitrogen and hydrogen gas mixture for 25 hours. During both technologies, the goal was to create a compound layer with a thickness of 10 µm and a diffusion layer with a thickness of 100 µm.

During aluminium pressure casting, molten aluminium at 650–700 °C was injected into the cavities of the casting tool, which often exceeded the speed of 30 m/s, at a pressure of up to 1300 bar [6]. The surface of the tool was exposed to strong

mechanical stress and severe corrosion effects. Damages caused by complex deterioration mechanisms are thermal fatigue, wear and corrosion.

During the research, the samples were subjected to cyclic heat and corrosion effects in a molten aluminium medium. The specimens were immersed in an aluminum medium at 700 °C for 5 minutes, then cooled in air for 5 minutes for 10 cycles.

After the surface treatment and corrosion testing, the samples were cut perpendicular to the surface. The mounted cross-section samples were sanded and polished. The samples have been given a name for ease of reference, as shown in [Table 2](#).

2.2. The test methods

Vickers hardness was measured on the samples in accordance with ISO 18203:2016, the standard for determining surface-treated crust thickness. First, the core hardness was measured from the average of three measurements taken in the middle of the samples.

After that, the additional measurement points were taken from the surface of the sample every 0.05 mm, in two measurement rows, offset by 0.025 mm from each other. A total of 20 measurements were made on one sample.

The mounted and polished samples were chemically etched with 2% Nital solution for 60–90 seconds, which made the microstructure visible and ready for further examinations.

Before the tests, performed with a Zeiss EVO MA 10 type scanning electron microscope (SEM), the surface of the sample embedded in the mounting resin was coated with a thin layer of gold, and then

Table 1. Chemical composition of the test specimens

C	Si	Mn	Cr	Mo	V
0.38	0.20	0.55	5.00	1.80	0.55

Table 2. Notations of the samples

Sample	Name
Reference	R1
Reference, cyclic heated	R2
Salt bath nitrided	S1
Salt-bath nitrided, cyclic heated	S2
Plasma nitrided	P1
Plasma nitrided , cyclic heated	P2

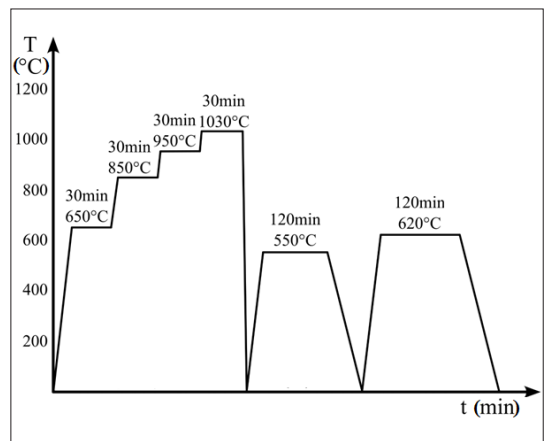


Fig. 1. Preliminary heat treatment of the samples.

the samples were attached to the sample holder with double-sided, carbon-based adhesive tape. The chemical composition of samples was determined by energy-dispersive X-ray spectrometry (EDS) during the electron microscopic examinations. During these tests, elemental analysis was performed on the individual samples, and the precipitates found on them, and the material quality of any compound layers that may have formed was determined.

3. The results of the tests

3.1. The results of the microhardness measurement

The results of the microhardness measurement are summarized in **Figures 2** and **3**.

Based on the results, it can be concluded that although the salt bath nitrided sample has a thicker diffusion zone, its hardness is lower than that

of the plasma nitrided sample. In the case of the samples treated in molten aluminium, a significant decrease can be seen in the hardness values. It was an average of 10% for the reference sample, an average of 6.3% for the salt-bath-treated sample up to a layer depth of 0.1 mm, and 17.8% for the plasma-nitrided sample..

3.2. The results of the examinations performed with a scanning electron microscope

Figure 4 shows the network structure formed in the case of the nitrided samples, which appears more strongly in the samples treated in the salt bath.

The white band visible on the surface of the samples was presumably the compound layer, but this can only be confirmed after elemental analysis. The nets appeared even more densely at the corners of the samples (**Fig. 5**).

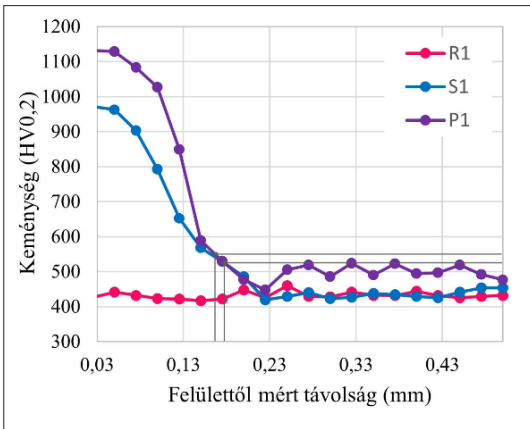


Fig. 2. Comparison of the results of each procedure before aluminium treatment.

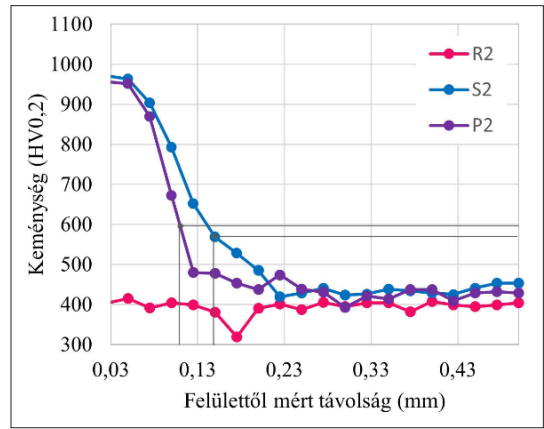


Fig. 3. Comparison of the results of individual procedures after aluminium treatment.

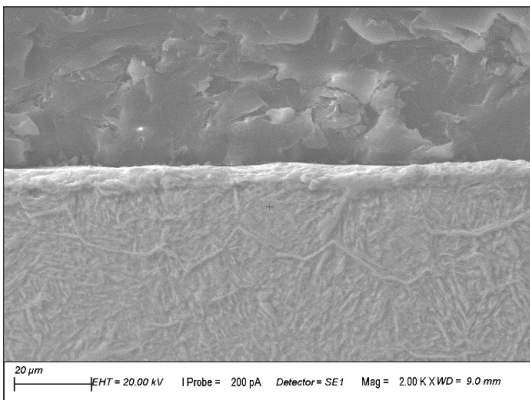


Fig. 4. Cross-sectional view of sample S1.

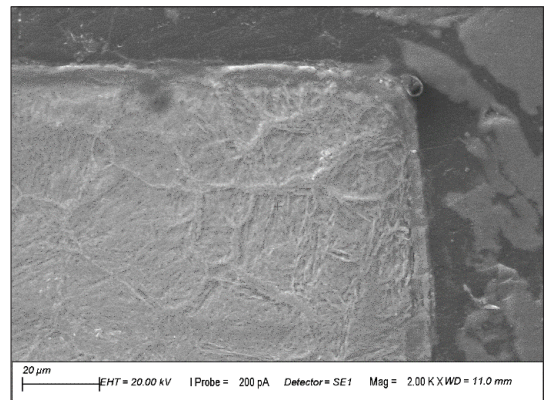


Fig. 5. Nitride structure formed on S2 sample's edge.

3.3. Results of energy dispersive X-ray spectrometry

Due to their high nitrogen content, the nitride structure visible on the sample's edges was nitride precipitation, which formed along the grain boundaries.

Along the corners, nitrogen was present in a higher mass percentage. This phenomenon can be attributed to the fact that at the corners of the samples, nitrogen has the opportunity to diffuse into the base material from several directions, due to the resulting local supersaturation, the excess amount of nitrogen appears in the form of precipitates along the grain boundaries [7].

This so-called edge effect was primarily observed during plasma nitriding. However, a higher nitrogen content can be detected in each nitrided sample. Based on the results of the EDS test, in the case of the plasma nitrided samples, this amount was almost twice the nitrogen content of the samples treated in the salt bath.

The corners of the nitrided samples are presumably harder due to the edge effect, but they are more brittle. This phenomenon was not desirable in all cases, as the hardened material can easily break off with tools subject to dynamic stress. However, due to their good tribological properties, hard edges have a good resistance to wear. During examination of the top surfaces of the nitrided samples, it was found that their nitrogen content was almost the same. A possible reason for this was that although the two processes were performed with different production parameters, the goal was to achieve the same diffusion and compound layer thickness in both cases. Nitrided samples with index 2 show a significant decrease in nitrogen content. The values measured on different samples and areas are illustrated in Table 3.

Based on the results, it can be concluded that while the nitrogen content of the salt bath samples decreased by only nearly 40%, the plasma

nitrided samples lost a much more significant amount of nitrogen, their nitrogen content decreased by 66–67%.

This phenomenon can be explained by the fact that the ϵ -nitrides formed during salt bath nitriding are presumably thermodynamically more stable and have better heat resistance [8].

The statement is also supported by the results obtained during the hardness measurement, where, in the case of the sample treated in the salt bath, the hardness level decreased to a much lesser extent because of heat cycling.

During decomposition, diffusion processes start towards areas poorer in nitrogen, which was the environment surrounding the test pieces. As a result, the nitrided layer became depleted in nitrogen. In contrast to the reference sample, complete dissolution of the base material or the nitrided layer on the surface of the test specimen that underwent both plasma and salt bath nitriding was not discovered.

4. Summary of results

The microhardness measurement tests determined the different hardnesses and layer depths achieved by each nitriding process. It can be concluded that the surface hardness of the plasma nitrided sample is higher, but the thickness of the formed layer is somewhat smaller than in the case of samples produced by the salt bath process.

After cyclic treatment in the aluminium bath, the electron microscopic examination showed that the nitrided layer protected both nitrided samples from the formation of intermetallic compounds. At the same time, in the case of both treatments, a significant change can be observed in the hardness of the samples and the thickness of the nitrided layer. In this regard, it can be concluded that after treatment, the sample nitrided in the salt bath suffered less damage in terms of both hardness and layer thickness during the cyclic heat load.

The elemental analysis supported the assumptions made in previous measurements, and we were able to make further findings regarding the composition of the samples. From the high nitrogen concentration of the nitride structure located on the edge of the samples, it can be concluded that the edge effect mainly affects plasma-nitrided samples.

In the case of nitrided samples suffering from corrosion in molten aluminium, we could make the statement that the sample treated in a salt

Table 3. Change in nitrogen concentration of individual samples

Sample	Nitrogen content (m/m%)		
	1	2	Δ (%)
S (on top surface)	4.6	2.8	39.1
S (corner)	5.7	3.5	38.6
P (on a top surface)	5.8	1.9	67.2
P (corner)	10.5	3.6	65.7

bath loses its nitrogen content to a lesser extent than the plasma nitrided piece. This was explained by the different thermodynamic stability of the different nitrides and the diffusion processes following the decomposition.

Acknowledgement

This work was supported by the National Research, Development and Innovation Office (NKFIH) under grant contract OTKA-PD_21 142307.

The project supported by the Doctoral Excellence Fellowship Programme (DCEP) is funded by the National Research Development and Innovation Fund of the Ministry of Culture and Innovation and the Budapest University of Technology and Economics, under a grant agreement with the National Research, Development and Innovation Office

References

- [1] Conci M. D., Bozzi A. C., Franco A. R.: *Effect of plasma nitriding potential on tribological behaviour of AISI D2 cold-worked tool steel*. *Wear*, 317/1–2. (2014) 188–193.
<https://doi.org/10.1016/j.wear.2014.05.012>
- [2] Dai M., Li C., Chai Y.: *Rapid Salt Bath Nitriding of Steel AISI 1045*. *Metal Science and Heat Treatment*, 60. (2018), 454–456.
<https://doi.org/10.1007/s11041-018-0300-8>
- [3] Hawryluk M., Dolny A., Mrozmski S.: *Low cycle fatigue studies of WCLV steel (1.2344) used for forging tools to work at higher temperatures*. *Archives of Civil and Mechanical Engineering*, 18. (2018) 465–478.
<https://doi.org/10.1016/j.acme.2017.08.002>
- [4] Kohli A. H., Hanief M., Jagota, V.: *A retrospection of the effect of nitriding processes on the AISI H13 tool steel*. *Advances in Materials and Processing Technologies*, 9/2. (2022) 425–440.
<https://doi.org/10.1080/2374068X.2022.2093012>
- [5] Yucel B.: *Response to thermal cycling of plasma nitrided hot work tool steel at elevated temperatures*. *Surface and Coatings Technology*, 205/2. (2010) 597–602.,
<https://doi.org/10.1016/j.surfcoat.2010.07.035>
- [6] Guang C., Jun W., Hongyuan F., Danqi W., Xiaoying L., Hanshan.: *Combat molten aluminum corrosion of AISI H13 steel by low-temperature liquid nitrocarburizing*. *Journal of Alloys and Compounds*, 776. (2019) 702–711.
<https://doi.org/10.1016/j.jallcom.2018.10.298>
- [7] Pye D.: *Practical Nitriding and Ferritic Nitrocarburizing*. ASM International, 2003.
<https://doi.org/10.31399/asm.tb.pnfn.9781627083508>
- [8] Fang C., van Huis M., Zandbergen H.: *Stability and structures of the ϵ -phases of iron nitrides and iron carbides from first principles*. *Scripta Materialia*, 64. (2011) 296–299.
<https://doi.org/10.1016/j.scriptamat.2010.08.048>



The Effects of Laser Power and Travel Speed on Weld Geometry in the case of Manual Laser Welding

Virág SIMON,¹ Balázs VARBAI,² Károly ABAFFY,³ László GYURA⁴

¹ Budapest University of Technology and Economics, Faculty of Mechanical Engineering, Department of Materials Science and Engineering, Budapest, Hungary, simon.virag240@gmail.com

² Budapest University of Technology and Economics, Faculty of Mechanical Engineering, Department of Materials Science and Engineering, Budapest, Hungary, varbai.balazs@gpk.bme.hu

³ Linde Gáz Magyarország Zrt. Budapest, Hungary, karoly.abaffy@linde.com

⁴ Linde Gáz Magyarország Zrt. Budapest, Hungary, laszlo.gyura@linde.com

Abstract

In our research, we investigated the effects of laser power and travel speed on the weld geometry in case of manual laser welding. Our experiments revealed that a characteristic two-part weld geometry is obtained under our experimental parameters. It was also found that increasing the laser power leads to a nearly linear increase in the weld width, while increasing the travel speed leads to a decrease in the weld width. The penetration depth does not increase further above a certain power level. A decrease in travel speed results in an increase in penetration depth. At the travel speeds tested, a narrow and deep weld geometry was obtained at the 70-80 % power level and a wider but shallower weld at the 90-100 % laser power level.

Keywords: manual laser beam welding, laser power, travel speed, weld geometry.

1. Introduction

Laser beam welding, after laser beam cutting, is the most widely used laser material processing technology, and its mechanised version is widely used in industry due to its many advantages [1]. The advantages of laser welding are the very low heat-affected zone created by the highly concentrated laser beam focused over a small area and the much lower heat input compared to conventional fusion welding processes, which minimises deformation of the workpiece by internal stresses [2, 3]. Its cost-effectiveness also makes it popular in industrial applications, as the high initial investment cost is quickly recovered due to its high processing speed and thus high productivity [4]. In recent years, hand-held laser welding equipment has also appeared on the market, offering user-friendly operation with a lightweight welding gun and working cable, and a small, easily movable beam source [5]. A growing number of companies are selling and using such equipment in Hungary, but due to its novelty, there is currently very little experience with this process.

In the present study, we investigated the effects of laser power and travel speed on the weld geometry in the case of manual laser beam welding of austenitic stainless steel.

2. Welding and evaluation procedure

In our research, two series of experiments, each consisting of 10 welds, were carried out on 2.7 mm wall thickness, 42 mm outer diameter, 1.4301 grade austenitic stainless steel tubes by manual laser beam welding without the addition of any welding filler metal.

In general, the chemical composition of the steel used is shown in **Table 1**.

Table 1. The chemical composition of the 1.4301 grade austenitic stainless steel [6]

C	Si	Mn	P	S
≤0.07	≤1.00	≤2.00	≤0.045	≤0.03
N	Cr	Ni	Fe	
≤0.10	17.5–19.5	8.0–10.5	rest.	

It should be highlighted that, in order to ensure the reproducibility of the welds during the experiments, the hand-held laser beam welding gun was enclosed in a device to ensure its stability, thus eliminating errors due to the unproven human hand. To ensure a uniform travel speed, the tube material was rotated by means of a rotating device.

Welding of the experimental series was carried out using an XTW-1000 type optical fibre hand-held laser beam welding machine manufactured by Jinan Xintian Technology Co. of China. The machine produces a laser beam with a wavelength of 1080 nm and can deliver a maximum power of 1000 W. The machine's control panel allows the laser power output to be set in percentage form. The first set of experiments was welded at 24 cm/min and the second set of experiments at 40 cm/min, with the laser power varied from 100% to 20% in 10% steps. Based on the experiences of our preliminary experiments, no weld is formed at 10% laser power, so the 10% power level was skipped from the present study. In addition to the power delivered, it is possible to select the wobbling mode of the laser beam within the gun and to adjust the frequency and amplitude of this movement. The laser beam is swung inside the welding gun by optically guiding the laser beam [7]. Our welds were made without swinging the laser beam. The shielding gas used was nitrogen of 4.6 purity at 2.5 bar.

To ensure that the position of the cross-sections tested was the same for all bead-on-plate welds, the specimens were cut in the same position along their longitudinal axis using a Struers Discotom-10 water-cooled disc cutter. The specimens

were then embedded and metallographic grindings were made. Starting with P600 sandpaper and moving to progressively finer grain-size paper, we arrived at P2500 sandpaper. To remove the fine scratches, the samples were polished using a suspension of 3 μm diamond grains. The seam geometry was developed by etching. The etching of the grindings was performed using Adler etchant with the following composition:

- 9 g copper ammonium chloride;
- 150 ml hydrochloric acid;
- 45 g ferric chloride 6-hydrate;
- 75 ml distilled water.

Using the etchant, the geometry of the welds was developed by etching the samples for 2-3 seconds at room temperature and then examining them under an Olympus SZX 16 stereo-microscope. Finally, photographs of the welds were taken using Stream Essentials software to measure the seam width and fusion depth values required for the evaluation. From these values, diagrams were drawn, with some microscopic images plotted as examples to illustrate the resulting weld geometries.

3. Results and evaluation

By observing the microscopic images shown in figures 1–2, it can be observed that the pointwise wobbling mode results in an interesting seam geometry consisting of two parts, a wider and shallower heat conducting part and a narrower and deeper deep seam part.

Figure 1. shows the resulting seam width as a function of laser power and travel speed. The graph shows that the seam width increases with increasing power at both speeds, but to dif-

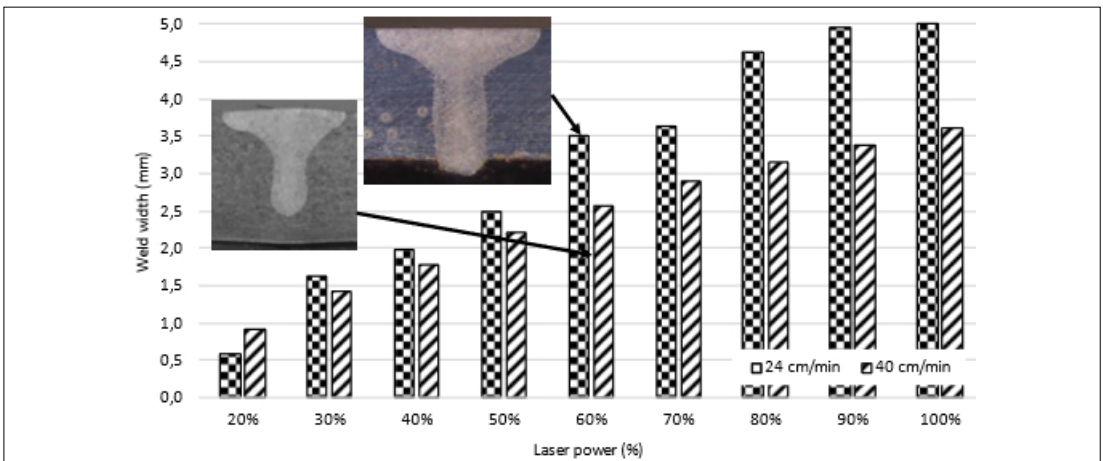


Fig. 1. Weld width as a function of laser power and travel speed.

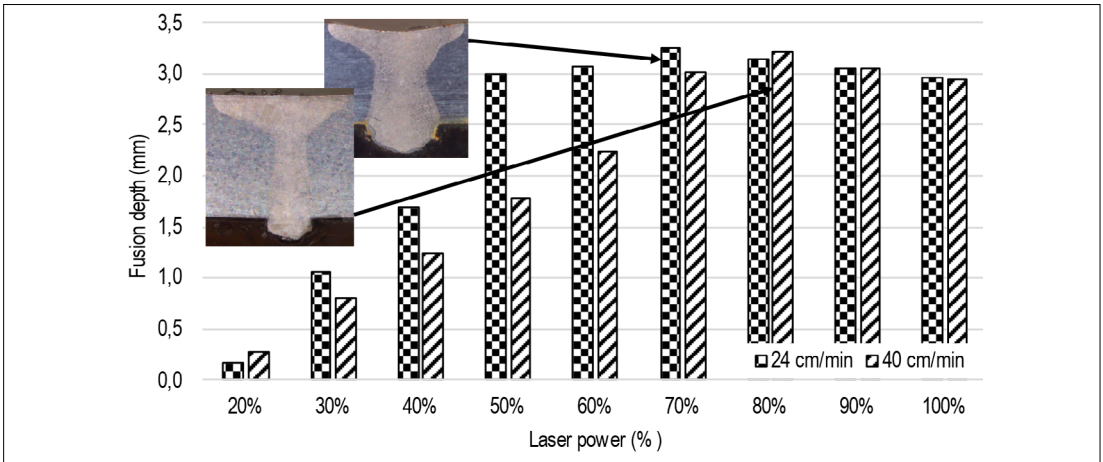


Fig.2. Fusion depth as a function of laser power and travel speed.

ferent extents, with a steeper - almost linear - curve at 24 cm/min and a flatter curve at 40 cm/min.

It can be concluded that both increasing the laser power and decreasing the travel speed will result in an increase of the seam width.

The inset micrographs clearly show that at the same power level, a higher travel speed leads to a smaller weld width.

Figure 2. plots the fusion depth as a function of laser power and travel speed. It can be said that the fusion depth is maximum at power levels of 70-80%, increases gradually at lower power levels and decreases again above 80%. It is interesting to observe that in the 70-80% power range, the welds with a much greater fusion depth were produced at 40 cm/min than at 24 cm/min, the former achieving a fusion depth of 5.91 mm, while the latter only achieved a fusion depth of 3.14 mm. Looking at the inset microscopic images and the data from the diagrams, it can be concluded that the weld geometries are slender and deep at 70-80% laser power and wider and shallower at 90-100%.

4. Conclusions

In the present study, bead-on-plate welds were welded by manual laser beam welding on austenitic stainless steel tubes to investigate the effects of laser power and travel speed on the weld geometry. Based on our results, the following conclusions can be drawn:

- by using a pointwise wobbling mode, two parts of the weld shape - a wider and shallower heat conducting part, and a narrower and deeper deep seam part - are formed;

- as the laser power is increased, the weld width increases almost linearly;
- increasing the travel speed leads to a decrease in the seam width;
- in the 70-80% power range, the fusion depth of a weld made at a travel speed of 40 cm/min exceeded that welded at a travel speed of 24 cm/min;
- at the test speeds, a slender and deep weld geometry was obtained at the 70-80% power level and a wider and shallower weld geometry at the 90-100% power level.

Acknowledgement

Linde Gáz Magyarország Zrt. provided us the necessary raw material and equipment for the experiments, which we would like to thank them for. The project was funded by the National Research, Development and Innovation Office - NKFIH (OTKA PD 138729).

References

- [1] Buza G.: *Lézersugaras technológiák I.* Edutus Főiskola, Tatabánya, 2012. 75.
- [2] Bitay E.: *Hegesztési alapismeretek.* Erdélyi Múzeum-Egyesület, Kolozsvár, 2021. 58. <https://doi.org/10.36242/mtf-16>
- [3] M. Reis, E. Şerifağaoğlu: *A Smart Handheld Welding Torch Device for Manual Spot Laser Welding.* Smart Manufacturing and Materials, II. (2022) 1.
- [4] ESAB Kft., Lézersugaras hegesztés. https://esab.com/hu/eur_hu/esab-university/blogs/what-is-laser-welding-and-how-does-the-technique-work/ (accessed on: 2024. febr. 26.).
- [5] V. Gapontsev, F. Stukalin, A. Pinard, O. Shkurikhin, Y. Grapov, I. Markushov: *Handheld laser welding and cleaning system for typical metal fabrication*

using 1.5 kW fiber laser source. Proceedings Volume 11981, Fiber Lasers XIX: Technology and Systems (2022) 1.

<https://doi.org/10.1117/12.2616585>

- [6] AGST Draht & Biegetechnik GmbH., Rozsdamentes acél 1.4301 adatlap.

<https://www.agst.de/4301?lang=hu> (accessed on: 2024. febr. 26.).

- [7] C. Yuce: *The Effect of Laser Beam Wobbling Mode on Weld Bead Geometry of Tailor Welded Blanks*. Published in 8th International Symposium on Innovative Technologies in Engineering and Science, (2020) 2.

Investigation of Friction Stir Welded Polycarbonate Plates

Róbert Gábor STADLER,¹ Richárd HORVÁTH²

¹ Doctoral School on Materials Sciences and Technologies, Óbuda University, Budapest, Hungary, stadler.robort@bgk.uni-obuda.hu

² Bánki Donát Faculty of Mechanical and Safety Engineering, Óbuda University, Budapest, Hungary, horvath.richard@bgk.uni-obuda.hu

Abstract

This study investigates how different input parameters (speed and feed rate) affect the force components during welding and weld strength. In addition, we used microscopic imaging to observe the welding defects that occurred and their effects on failure. The measurement results show that welding forces decrease with increasing tool speed. The highest weld strength (28.5 MPa) was obtained at 1000 rpm and a feed rate of 8 mm/min.

Keywords: friction Stir Welding, polycarbonate, welding force, joint efficiency.

1. Introduction

Today, polymers are widely used in various industries. As these materials spread, we need high-quality economical joining technologies. As in the case of metals, the most commonly used bonding technology with polymers is also welding. Due to its wide industrial application, ultrasonic welding [1], laser welding [2], and friction stir welding [3] of polymers are still popular research fields.

Friction stir welding is a welding technology based on friction, patented in the early 90s [4]. During the process, a rotating tool is guided along the line where the plates are to be joined. Friction occurs between the tool and the plates, which produces the temperature required for welding and the formation of the seam. Friction stir welding can produce a high-quality bond, and is also economical, environmentally friendly and energy-efficient [5].

Although at an industrial level, it is mostly used for aluminium, the possibility of using it on polymers has been researched since the beginning of the 2000s. [6]. In addition to the advantages mentioned above, tests have proved that the technology is suitable for welding thicker polymer sheets and welding of thermoplastic polymer matrix composites [7].

Figure 1 shows the schematic diagram of friction stir welding and the force components during the process.

Polycarbonate (PC) is widely used in the automotive, construction and healthcare industries [9]. It has excellent mechanical and thermal properties, and is also one of the few polymers that can be produced in water-clear or optical quality.

Due to its wide range of applications and its water-clear property, many publications have focused on stir-friction welding tests of polycarbonate (PC) in recent years.

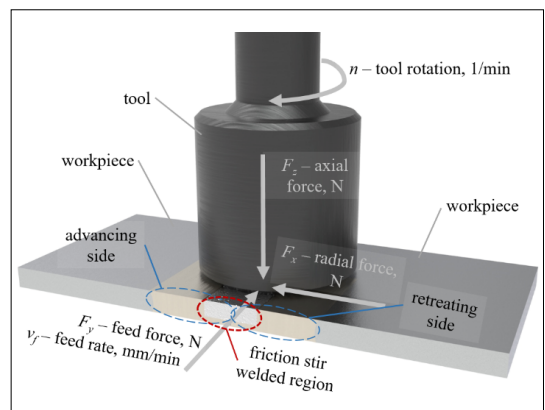


Fig. 1. A schematic diagram of friction stir welding. [8]

Derazkola et al. [10] investigated the joining of polycarbonate (PC) plates by friction stir welding. The purpose of the study was to find a correlation between the welding parameters and the mechanical properties of the seam. They welded 4 mm thick PC plates. During the welding experiments, tool speed, feed rate, tool depth and tool angle were changed. After the welding tests, tensile strength, hardness and specific fracture energy were tested. The best tensile strength (55 MPa) and flexural strength (61 MPa) were achieved with 2200 1/min, a feed rate of 105 mm/min, a tool inclination angle of 2,5° and a tool depth of 1.2 mm.

Ahmed et al. [11] also investigated the friction stir welding of PC plates. They used three rotational speeds (1000, 1500 and 2000 1/min) and four feed rates (25, 50, 75 and 100 mm/min). With most parameters they managed to produce seams without defects. The best tensile strength (66 MPa) was achieved with a rotational speed of 1500 1/min and a feed rate of 50 mm/min, and a rotational speed of 1000 1/min and a feed rate of 50 mm/min.

Lambiase et al. [12] friction stir spot welded PC plates. They used three rotational speeds (2000, 4000 and 6000 1/min), and five feed rates (20, 40, 60, 80 and 100 mm/min). Their results showed that a high feed rate makes the seam thin. They achieved the highest tensile strength (32 MPa) with a feed rate of 60 mm/min.

Vidakis et al. [13] friction stir welded 4 mm thick PC sheets. They measured the force components during welding. In addition to the welding parameters, they also varied the diameter of the pin and shoulder. The morphological characteristics of the seams were examined with an optical microscope, while the porosity of the seams was examined by micro-computer tomography. Their results indicated that a low feed rate reduces the porosity of the seam and affects its dimensional accuracy. Also, a low feed rate and high rotation speed reduce the forces in the process.

Kumar et al. [14] examined the weldability of polycarbonate (PC) and acrylonitrile butadiene styrene (ABS). They welded together 6 mm thick PC and ABS plates. They used three different rotational speeds (800, 1200 and 1600 1/min), feed rates (6, 12 and 18 mm/min) and tool angles (0, 1 and 2°). The tool had a threaded geometry. They found that tensile strength increases as rotational speed and the inclination angle of the tool are increased. The best tensile strength was achieved with a feed rate of 12 mm/min (22,42 MPa).

In this study, we investigate the friction stir welding of 4 mm thick PC sheets. The force components during welding and the strength of the seams are examined as a function of the input parameters. We also examine welding defects.

2. Materials and methods

During the tests, 4 mm thick optical quality DO-CANAT clear 099 (Quattroplast Kft., Budapest, Hungary) plates were welded together. The welding test specimens were cut to an overall size of 90×110 mm, so after welding, we were able to cut the standard flat tensile test specimens from the samples. **Figure 2.** shows the cutting and numbering of the welding test specimens.

The welding tests were performed on a MAZAK Nexus VCN 410A-II CNC milling machine. The force components during welding (F_x , F_y , F_z , – **Figure 1**) were measured with a Kistler9257B piezoelectric force meter clamped under the machine vice. The range of the force meter is $F_x = F_y = -5...5$ kN and $F_z = -5...10$ kN [15].

Using the three measured force components, we calculated the resultant force during welding as follows:

$$F_e = \sqrt{F_x^2 + F_y^2 + F_z^2} \quad (1)$$

The tensile tests of the 3 tensile specimens per measurement point was performed with a Zwick Z005 tensile tester at a test speed of 10 mm/min. We recorded images of the welding seams with a Dino-lite AM3113T type microscope.

The tool used during the welding tests was chosen based on the literature [13]. The geometry of the pin was cylindrical. The diameter of the pin was 4 mm, while the diameter of the shoulder was 10 mm, and the material of the tool was C45 steel. The welding tool used is shown in **Figure 3.**

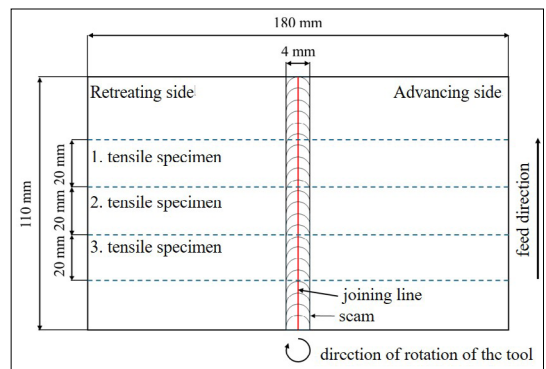


Fig. 2. The cutting and numbering of the welding test specimens.

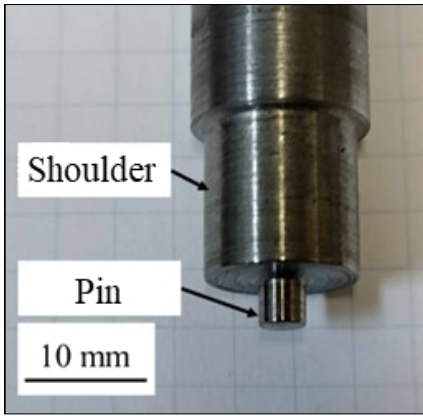


Fig. 3. The welding tool used.

Table 1. Welding parameters

Parameters		Levels		
		-1	0	1
x_1	rotational speed – n , 1/perc	600	800	1000
x_2	feed rate – v_p , mm/perc	6	8	10

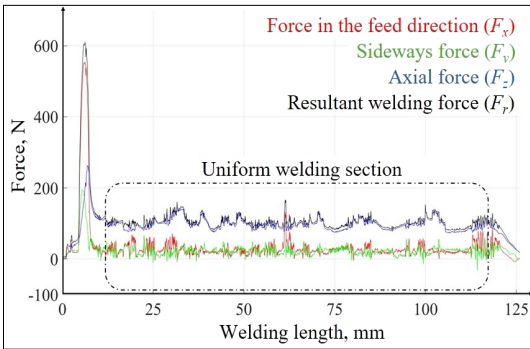


Fig. 4. Force components during welding.

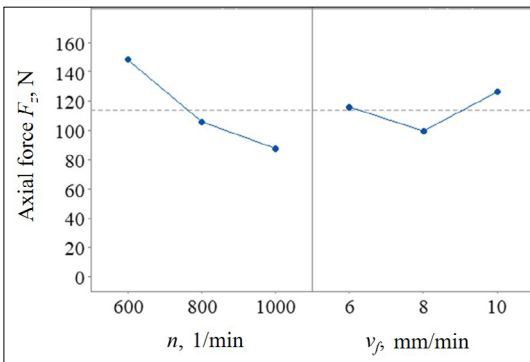


Fig. 5. The effect of the welding parameters on axial force (F_z).

AWe used three different rotational speeds and feed rates. The parameters were determined based on preliminary experiments and the literature (Table 1).

We used a full design of experiments (all parameter combinations).

3. Results

3.1 Analysis of the registered forces

Figure 4 shows the forces during welding. In addition to the three force components (F_x , F_y , and F_z) we showed the resultant force (F_r) too. There is no significant sideways (F_x) or force in the feed direction (F_y). The greatest force is axial force (F_z) so this affects the resultant force most (F_r). For all three force components, the forces can be divided into three sections during welding. An initial section, where forces increase suddenly, as the tool enters the welding zone, then welding with uniform forces and a decreasing section as the tool leaves the welding zone.

During the evaluation of forces, we always evaluated the average forces in the uniform welding section because this characterizes the welding process best

3.2. The results of the evaluation of forces

There is very little sideways force (F_x) and force in the feed direction (F_y) during welding. Therefore, we examined the axial force component (F_z) and the resultant welding force (F_r).

Figure 5 shows the effect of the axial force (F_z) depending on welding parameters. As rotational speed increases, forces decrease. This can be observed in the friction stir welding of other polymer materials as well [8, 13, 16]. As rotational speed is increased, the temperature in the welding zone increases, and the polymer material exerts less resistance on the welding tool. Feed rate has less influence on the axial force (F_z), than the rotational speed of the tool.

Figure 6 shows the main effects plots of F_e Fe as a function of welding parameters. Since the dominant force during welding is the axial force (F_z) the tendencies are similar here, too. As rotational speed increases, the force component decreases.

3.3. The results of strength tests

The seams were characterized with their tensile strength. We cut 3 tensile specimens from each welding sample and performed tensile tests on the specimens. The average of the three tensile tests were considered. Figure 7 shows the aver-

age tensile strength of each measurement point and the standard deviation of the three tensile strengths.

The greatest seam strength was achieved with a tool rotational speed of 1000 1/min and a feed rate of 8 mm/min: average tensile strength was 28.5 MPa. The lowest seam tensile strength was 4.2 MPa with 1000 1/min and 6 mm/min.

The greatest seam strength was always obtained with a feed rate of 8 mm/min. Also, standard deviation was rather high, which can be attributed to welding defects in the seams.

3.4. The analysis of welding defects

Figure 8 shows a typical seam from a top view. In addition to the pin, the shoulder also plays an important role in creating the seam. The seam is not optical quality. At the border of the shoulder, burr formed at every measurement point.

To analyse welding defects and their effects, we produced microscopic images of the cross-sections of the tensile specimens before and after the tensile test. In the cross-sectional image of the measurement point of the lowest tensile strength ($n = 1000$ 1/min and $v_f = 6$ mm/min) a tunnel defect was clearly visible (Figure 9). The tunnel defect is a part with significant material loss along the seam [17]. The defect occurred in the retreating side and probably greatly reduced strength. Figure 10 shows the microscopic image of the specimen after the tensile test, where it is clearly visible that failure occurred along the tunnel defect.

At higher RPMs, the seam became thinner, which is also a typical defect in friction stir welding [17]. In this case, the thickness of the plate is reduced below the original thickness (Figure 11).

4. Conclusions

In this article, we performed a friction stir welding tests of 4 mm thick polycarbonate (PC) sheets. During the welding process, we measured the forces in 3 directions, from which we calculated the resultant welding force, and also examined the measured forces during the welding process. The quality of the seams was characterized with a tensile test. The welding defects were examined with a microscope. Based on our results, we arrived at the following conclusions:

- The force characterizing the welding process can be divided into three sections: initial section, when the force increases; a steady section with a uniform force; and a final section, when the force decreases.

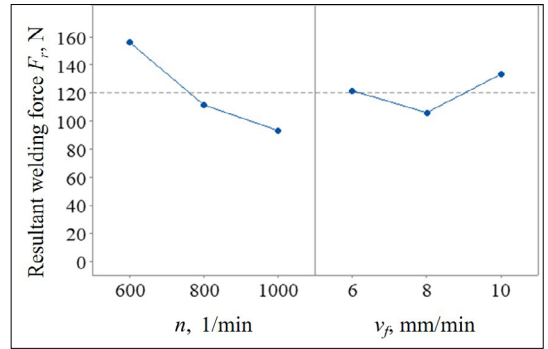


Fig. 6. The effect of the welding parameters on resultant force (F_r).

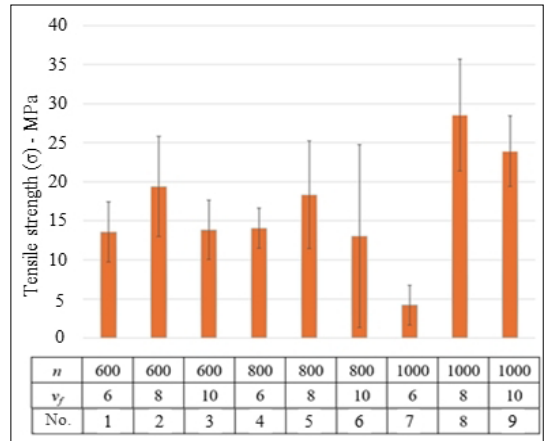


Fig. 7. The effect of welding parameters on the strength of the seam.



Fig. 8. A characteristic seam from a top view.

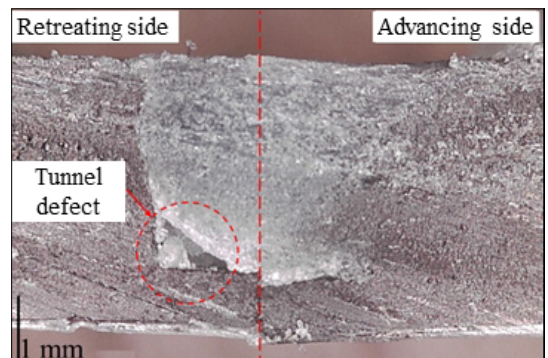


Fig. 9. Tunnel defect at measurement point 7.



Fig. 10. 7th measurement point – specimen after the tensile test

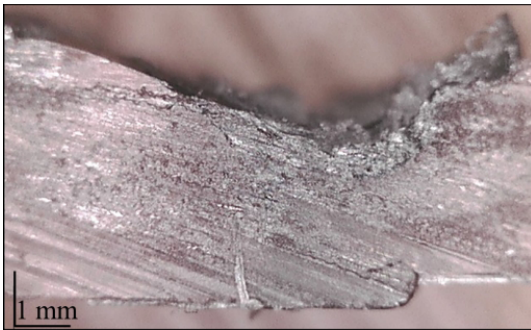


Fig. 11. Seam thinning.

- Among the forces during welding, the axial force (F_z) is dominant and this affects the resultant force most.
- As tool rotational speed is increased, both the axial force (F_z) and the resultant force (F_r) decrease.
- We obtained the highest tensile strength with a tool rotational speed of 1000 1/min and a feed rate of 8 mm/min (28.5 MPa), and the lowest tensile strength (4.2 MPa) with a rotational speed of 1000 1/min and a feed rate of 6 mm/min.
- The microscopic images showed tunnel defects and seam thinning in several measurement points

Acknowledgements

Supported by the ÚNKP-23-3 New National Excellence Program of The Ministry for Culture and Innovation from the Source of The National Research, Development and Innovation Fund.

References

- [1] Kiss Z., Temesi T., Bitay E., Bárány T., Czigány, T.: *Ultrasonic welding of all-polypropylene composites*. Journal of Applied Polymer Science, 137/24. (2020) 48799. <https://doi.org/10.1002/app.48799>
- [2] Temesi T., Czigany T.: *The effect of surface treatment on the shear properties of aluminium-polypropylene joints manufactured by laser beam*. Polymer Testing, 117. (2023) 107882. <https://doi.org/10.1016/j.polymertesting.2022.107882>
- [3] Tiwari S. K., Sharma H., Rao A. U.: *A comprehensive review of the recent developments in friction stir welding of metals, alloys, and polymers: a review of process parameters and properties*. Journal of Adhesion Science and Technology, (2024) 1–24. <https://doi.org/10.1080/01694243.2024.2334271>
- [4] Thomas W. M., Nicholas E. D., Needhan J. C., Murch M. G., Temple-Smith P., Dawes C. J.: *International patent application PCT/GB92/02203 and GB patent application 9125978.8*. UK Patent Office, London 6, 1991.
- [5] Majeed T., Wahid M. A., Alam M. N., Mehta Y., Siddiquee A. N.: *Friction stir welding: A sustainable manufacturing process*. Materials Today: Proceedings, 46. (2021). 6558–6563. <https://doi.org/10.1016/j.matpr.2021.04.025>
- [6] Nelson T. W., Sorenson C. D., Johns C. J.: *Friction stir welding of polymeric materials*. Brigham Young University, Provo, UT, USA, US 6, 811,632 B2, 2004.
- [7] Czigány T., Kiss Z.: *Friction stir welding of fiber reinforced polymer composites*. In Proceedings of the 18th International Conference on Composite Materials. Jeju, South Korea, ICCM, 2011, August. 21–26.
- [8] Stadler R. G., Horváth R.: *Investigation of Welding Forces and Weld Strength for Friction Stir Welding of Acrylonitrile-Butadiene-Styrene (ABS) Plates*. Acta Materialia Transylvanica, 6/1. (2023) 53–58. <https://doi.org/10.33924/amt-2023-01-09>
- [9] Gohil M., Joshi, G.: *Perspective of polycarbonate composites and blends properties, applications, and future development: A review*. Green Sustainable Process for Chemical and Environmental Engineering and Science, (2022) 393–424. <https://doi.org/10.1016/B978-0-323-99643-3.00012-7>
- [10] Derazkola Hamed Aghajani, Simchi Abdolreza, Lambiasi Francesco: *Friction stir welding of polycarbonate lap joints: Relationship between processing parameters and mechanical properties*. Polymer Testing, 79, 105999, 2019, Elsevier. <https://doi.org/10.1016/j.polymertesting.2019.105999>
- [11] Ahmed M. M. Z., Elnaml A., Shazly, M, El-Sayed Seleman M. M.: *The effect of top surface lubrication on the friction stir welding of polycarbonate sheets*. International Polymer Processing, 36/1. (2021) 94–102, , De Gruyter <https://doi.org/10.1515/ipp-2020-3991>
- [12] Lambiasi F., Grossi V., Paoletti A.: *Advanced mechanical characterization of friction stir welds*

- made on polycarbonate. The International Journal of Advanced Manufacturing Technology, 104. (2019) 2089–2102, Springer
<https://doi.org/10.1007/s00170-019-04006-4>
- [13] Vidakis N., Petousis M., David C., Sagris D., Mourtakakis N., Moutsopoulou A.: *The impact of process parameters and pin-to-shoulder ratio in FSW of polycarbonate: welding forces and critical quality indicators*. The International Journal of Advanced Manufacturing Technology, (2024) 1–21.
<https://doi.org/10.1007/s00170-024-13033-9>
- [14] Kumar Sudhir, Roy Barnik Saha: *Novel study of joining of acrylonitrile butadiene styrene and polycarbonate plate by using friction stir welding with double-step shoulder*. Journal of Manufacturing Processes, 45. (2019) 322–330.
<https://doi.org/10.1016/j.jmapro.2019.07.013>
- [15] KISTLER Multicomponent Dynamometer 9257b datasheet, 2009, Kistler Group
- [16] Stadler G. R., Szebényi G., Horváth R.: *Investigation of weld forces and strength of friction stir welded polypropylene*. Periodica Polytechnica Mechanical Engineering, 67/3. (2023) 183–189.
<https://doi.org/10.3311/PPme.21899>
- [17] Huang Y., Meng X., Xie Y., Wan L., Lv Z., Cao J., Feng J.: *Friction stir welding/processing of polymers and polymer matrix composites*. Composites Part A: Applied Science and Manufacturing, 105. (2018) 235–257.
<https://doi.org/10.1016/j.compositesa.2017.12.005>

Tensile Testing of Bolted Joints in Pultruded Glass Fibre Reinforced Plastic Profiles

Valentin Endre SZABÓ,¹ Krisztián KUN²

¹ John von Neumann University, GAMF Faculty of Engineering and Computer Science, Department of Innovative Vehicles and Materials, Kecskemét, Hungary. szabo.valentin@nje.hu

² John von Neumann University, GAMF Faculty of Engineering and Computer Science, Department of Innovative Vehicles and Materials, Kecskemét, Hungary.

Abstract

Machine manufacturing and the automotive industry are often faced with supply chain problems for the raw materials used in the largest proportion (steel and aluminium) and the resulting large price changes. One solution to the lack of raw materials could be the introduction of new materials. Glass-fibre-reinforced plastic (GRP) profiles produced by pultrusion can be suitable for replacing metallic materials in many applications. However, one of the reasons for their limited distribution is the lack of well-established joining processes. The aim of the research is to test the tensile strength of the bolted connection of GRP sheet materials of different thickness according to an experimental design. Based on the experimental results, bolted joint recommendations can be provided for the examined GRP sections.

Keywords: GRP, pultrusion, bolted joint, failure.

1. Introduction

Pultrusion technology is a manufacturing process that produces composite profiles reinforced with longitudinal and continuous fibres. The reinforcing fibre material is most commonly glass or carbon fibre, although there are also natural fibre reinforcements available. The matrix material is usually a resin, typically polyester or epoxy. In the Pultrusion manufacturing process, the reinforcing fibres are first drawn into a resin bath. Then, the fibres and resin are pulled together through a heated mould designed to create the desired geometry. The matrix material gradually cross-links within the mould, and the resulting composite is cut to the appropriate length as it exits the mould. **Figure 1** illustrates the manufacturing process.

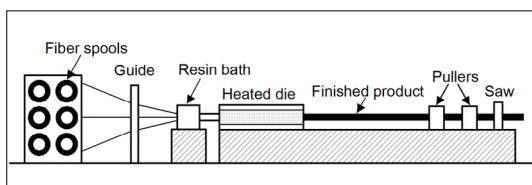


Fig. 1. The pultrusion manufacturing process [1]

The pultrusion process offers several advantages over other composite manufacturing processes, including the ability to produce profiles with consistent cross-sectional dimensions and properties, high strength-to-weight ratios, and tailored mechanical properties. Additionally, the process is highly automated and can be scaled up for high-volume production. However, there are also several challenges associated with pultrusion, such as the potential for voids or defects in the resulting composite and limitations on the complexity of the profiles that can be produced [1].

Pultrusion technology allows for the cost-effective and precise manufacturing of profiles with unique cross-sections that are otherwise not possible or difficult to produce using conventional materials. The design of an efficient profile geometry and structure can be achieved by determining the fibre composition and orientation based on known load direction and type. The mechanical properties of fibre-reinforced composite sections are dependent on the percentage by volume of the reinforcing fibres. This technology has become increasingly popular in the construction industry; however, the lack of a mature bonding

technology is the only obstacle to its rapid expansion. Two possible bonding technologies are the adhesive- and the bolted bonding. The moulding tool is treated with a mould release agent. From here, this material can be transferred to the profiles. This results in a low surface energy that is not favourable for adhesive joints, requiring surface treatment (cleaning) before bonding. The bolted bonding is more typical for GRP profiles than adhesive bonding [2, 3].

Due to the fibre reinforcement, the mechanical properties of glass fibre reinforced polymer profiles approach the load-bearing capacity of structural steels in the fibre direction, but the transverse load-bearing capacity can be an order of magnitude lower depending on the construction. The critical property of sections is, therefore, transverse strength. The holes required for bolted bonding tear the fibres. The orientation of the fibres, their location, and the spacing of discontinuities must be considered when designing the bonding technology to ensure resistance to tensile and bending stresses. These factors fundamentally affect the mode of failure. Our research aims to investigate the quality and failure modes of twist bonding of GRP profiles of varying thicknesses [4, 5].

2. Failures of bolted joints in GRP profiles

Prior to the tests, based on a review of the literature, the possible failures occurring in the bolted connection of the GRP profiles were summarized. The possible failure modes are shown in Figure 2. During profile examination, several types of failure may occur, which are primarily influenced by hole placement.

Bearing type failure is a common type of failure that can occur at the edge of a bore, where the fastener comes into contact with the base material. It typically occurs when the bore position is chosen poorly and is characterized by failure of both the base material and the fastener (Figure 1). Net-tension failure, on the other hand, occurs when the bore diameter and the fastener are too large in relation to the width of the base material, resulting in cracking of the sheets in the transverse direction, with the base material tearing. Shear-out failure is caused by shear stresses and typically occurs in the main loading directions at the boundary of the hole caused by the fastener, when the fastener diameter is too small and is usually accompanied by damage to the fastener. Finally, cleavage failure occurs as an outgrowth

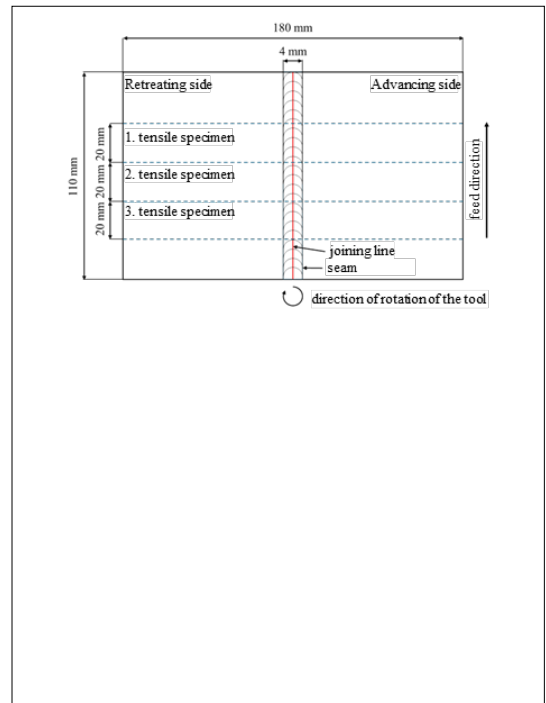


Fig. 2. Failure modes: a) Plastic deformation b) Net-tension c) Shear-out d) Cleavage [4]

failure and typically occurs in flat sections when the bore position tolerance is inadequate, leading to rupture and shear occurring together [6, 7].

3. Experimental conditions, measurements and results

In this chapter, the geometric design of the test specimens and the assembly required for the experiment are described. Additionally, the compiled experimental plan is presented.

3.1. The design of test specimens, experimental design

During the experiments, the overlapped GRP plates were fastened to each other with bolts. Figure 3 shows the geometric parameters of the GRP plates. During the series of experiments, the length (L) and width (W) of the specimens were not changed. Variable parameters were the thickness of the base material (t), the diameter of the fasteners and the hole (d_p), the distance between the holes (b) and the distance from the edge of the base material (a) [6, 8, 9].

During the tensile test, uniaxial tensile stress had to be provided so that the load force (F) exerted by the tensile machine was applied to the centre plane of the joint. In the case of overlap-

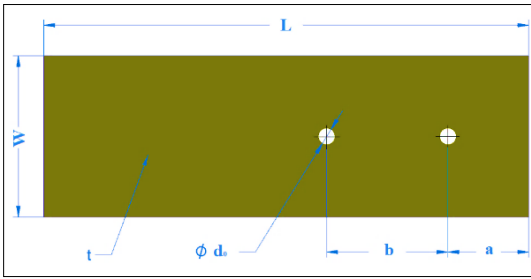


Fig. 3. Geometry of GRP profiles.

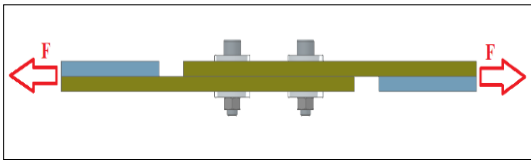


Fig. 4. Assembly suitable for tensile testing.

Table 1. Summary of the experimental design, determination of the experimental constants and variables.

Experimental	Specimen dimensions			Hole dimensions			Bolt dimensions		
	Thickness t (mm)	Width W (mm)	Length L (mm)	Front distance a (mm)	Middle distance b (mm)	Diameter d_0 (mm)	Bolt size	Tightening torque (Nm)	
1	t_1	4	50	500	25	37,5	4.1	M4	3
2	t_2	6							
3	t_3	10							
4	t_1	4	50	500	50	75	5,2	M5	6
5	t_2	6							
6	t_3	10							
7	t_1	4	50	500	100	150	6,4	M6	10
8	t_2	6							
9	t_3	10							

ping joints, this can be ensured by using a joint washer of the same thickness as the base material (Figure 4).

The experimental variables required for the experiment were determined based on a review of the current international literature on the research topic. A summary of the experiments is shown in Table 1. [6, 10]. Three tensile tests were performed. The bolts used for the tests were in

accordance with the MSZ EN ISO 4014 standard and had a strength class of 8.8. The bolt nuts were standard MSZ EN ISO 4034 and had a strength class of 8. Washers made of stainless-steel flat washers according to MSZ EN ISO 7094 were used. This was necessary to distribute the load on the surface of the GRP profiles as effectively as possible. The tightening torque of the bolts was based on a review of the literature. G. J. Turvey observed in his research that the quality of the joint is influenced by the tightening torque of the bolts. Therefore, the tests were carried out in a finger-tight state, the values are listed in Table 1 [4, 6, 7]

3.2. Mechanical testing of the raw material

The bond strength of the specimens was tested on an INSTRON 5800R 4482 universal material testing machine in accordance with the relevant standards. As a reference measurement, the tensile strength of the base material was also measured. During the tensile test of the base material, the following results were measured: the 4 mm thick GRP sheet ruptured at 50 kN, the 6 mm thick sheet at 75 kN and the 10 mm thick sheet at 95 kN.

3.3. Mechanical testing of the test specimens

Based on the experimental design, three tensile tests per series of experiments were performed. The experiments resulted mainly in bearing type failures. At 6 mm and 10 mm thickness, the bolts were found to be weak, as nearly identical values were measured during the experiments. The failure modes were also the same, in all cases the fasteners were trimmed. At 10 mm plate thickness, the hole was only damaged when using an M6 bolt, but this was barely noticeable. At 6 mm plate thickness, the use of an M6 bolt resulted in noticeable hole deformation, i.e. bearing-shaped failure, but the tensile force amplified the shear of the bolt. When using M5 and M4 bolts, the shear of the bolts was clearly measured.

Different results were obtained for a plate thickness of 4 mm. Table 1 shows the number of experiments as 1, 4 and 7. In each of these series of experiments, three were measured and the results are shown in Figure 5. The figure shows that, compared to the M4 bolt, the M5 can withstand 218% more load and the M6 260% more load. Compared to the M5 bolt, the M6 could withstand 119% more load. This result is consistent with the literature finding that the highest bond strength is associated with bearing type failure. For the 4mm GRP plate, the M4 bolts suffered shear fail-

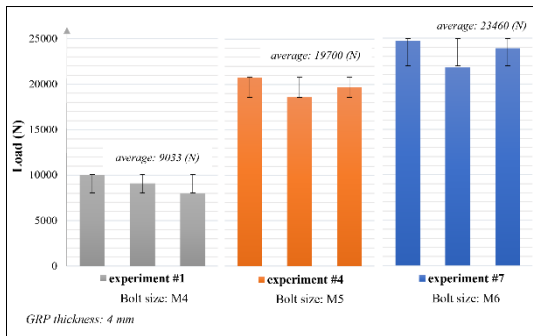


Fig. 5. Tensile test results for GRP plates.

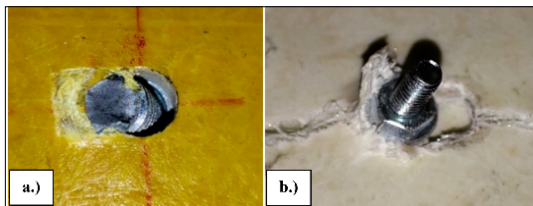


Fig. 6. a) Bearing type failure with sheared fastener ($t=6$, M6 bolt)
b) Shear type failure ($t=4$ mm, M5 bolt).

ures, while the M5 and M6 bolts suffered mixed, but increasingly bearing-like failures. By increasing the diameter of the bolts, increasingly higher bond strength was achieved, but there is an upper limit to this when the hole required for the bond diameter breaks too much glass fibre, and the failure mode is Shear-out or Cleavage as shown in Figure 2 (c and d). The bond strength would then show a downward trend again..

During the series of experiments, we observed two typical failures (Figure 6). More common is the bearing type (Figure 6.a), which in all cases was connected with a sheared fastener, but the raw material was damaged to varying degrees. The other is shear failure, which only occurred with a plate thickness of 4 mm (Figure 6.b). During this failure, the fastener was torn from the base material (without significant damage to the fastener).

4. Conclusion

During the experiments, two typical failure types were observed. Based on research in the literature, bearing failure ensures the greatest power transmission. In the case of the 10 mm thick GRP plates, the fasteners used proved to be inadequate, as the failure of the test specimen was always caused by the shearing of the fasteners. Therefore, further research is needed here.

For the 6 mm thick plates, the M4 and M5 bolts were also cut, and the hole was not significantly damaged. For the M6 screw, the hole shown in Figure 6.a showed slight deformation, but the measurement results show clear shearing of the fastener. These results suggest that even with a plate thickness of 6 mm, further tests will be needed with M6 and larger fasteners.

Different results were obtained when testing 4 mm GRP sheets. The use of the M4 fastener resulted in the lowest bond strength with shear-out failure alone (Figure 6.b). The fastener remained almost intact and was torn from the material. The M5 and M6 bolts showed a mixed shear-out and bearing failure pattern, but the fastener was not significantly damaged. Based on the results (Figure 5), it is not recommended to use M4 or smaller bolts for a 4 mm thick GRP plate. When M5 bolts were used, a 218% increase in bond strength was measured compared to M4 bolts. It can be seen that a larger screw diameter results in a more favourable bond strength, but there is an upper limit to this. Too many fibre breaks result in lower bond strength.

Overall, it can be stated that our results can be used as basic data for future research. It would be advisable to carry out a new series of experiments for each plate thickness, using fasteners with a larger diameter. In this way, a technological recommendation could be developed for every material thickness.

Acknowledgements

The research presented in this article was funded by the grant 2020-1.1.2-PIACI-KFI-2020-00052. The project was carried out under a call for proposals launched by the Ministry of Innovation and Technology through the National Research, Development and Innovation Office.

References

- [1] Barkanov E., Akishin P., Emmerich R., Graf. M.: *Numerical simulation of advanced pultrusion processes with microwave heating*. In Proceedings of the VII European Congress on Computational Methods in Applied Sciences and Engineering. 2016, vol. 4. 7720–7738). <https://doi.org/10.7712/100016.2368.5953>
- [2] Gallegos C., Marco F.: *Theoretical and Experimental Performance Analysis of a Cellular GFRP Vehicular Bridge Deck*. 2016. <https://doi.org/10.13140/RG.2.1.1737.6887>
- [3] Coelho A. M. G., Mottram J. T.: *A review of the behaviour and analysis of bolted connections and joints in pultruded fibre reinforced polymers*. Ma-

- terials & Design, 74. (2015) 86–107.
<https://doi.org/10.1016/j.matdes.2015.02.011>
- [4] Bank L. C.: *Composites for construction: structural design with FRP materials*. John Wiley & Sons, 2006. ISBN-13: 978-0471-68126-7
- [5] Ramful R.: *Failure Analysis of Bamboo Bolt Connection in Uniaxial Tension by FEM by Considering Fiber Direction*. Forest Products Journal, 71/1. (2021) 58–64.
<https://doi.org/10.13073/FPJ-D-20-00066>
- [6] Turvey G. J.: *Single-bolt tension joint tests on pultruded GRP plate – effects of tension direction relative to pultrusion direction*. Composite structures, 42/4. (1998) 341–351.
[https://doi.org/10.1016/S0263-8223\(98\)00079-8](https://doi.org/10.1016/S0263-8223(98)00079-8)
- [7] Turvey G. J., Sana A.: *Pultruded GFRP double-lap single-bolt tension joints – temperature effects on mean and characteristic failure stresses and knock-down factors*. Composite Structures 153. (2016) 624–631.
<https://doi.org/10.1016/j.compstruct.2016.06.016>
- [8] Tajeuna T. A., Légeron F., Langlois S., Labossiere P., Demers M.: *Effect of geometric parameters on the behavior of bolted GFRP pultruded plates*. Journal of Composite Materials, 50/26. (2016) 3731–3749.
<https://doi.org/10.1177/0021998315625101>
- [9] Wang Y.: *Bearing behavior of joints in pultruded composites*. Journal of composite materials, 36/18. (2002) 2199–2216.
<https://doi.org/10.1177/0021998302036018535>
- [10] Mottram J. T., Zheng Y.: *State-of-the-art review on the design of beam-to-column connections for pultruded frames*. Composite structures, 35/4. (1996) 387–401.
[https://doi.org/10.1016/S0263-8223\(96\)00052-9](https://doi.org/10.1016/S0263-8223(96)00052-9)